nature portfolio

https://doi.org/10.1038/s41586-022-05540-0

Supplementary information

Operando studies reveal active Cu nanograins for CO_2 electroreduction

In the format provided by the authors and unedited

Supplementary Information

Operando studies reveal active Cu nanograins for CO_2 electroreduction

Yao Yang[1,2,3,11], Sheena Louisia[1,3,11], Sunmoon Yu[3,4,11], Jianbo Jin[1], Inwhan Roh[1,3], Chubai Chen[1,3], Maria V. Fonseca Guzman[1,3], Julian Feijóo[1,3], Peng-Cheng Chen[1,5], Hongsen Wang[6], Christopher J. Pollock[7], Xin Huang[7], Yu-Tsun Shao[8], Cheng Wang[9], David A. Muller[8,10], Héctor D. Abruña[6,10] & Peidong Yang[1,3,4,5,*]

[1]Department of Chemistry, University of California, Berkeley, CA 94720, USA.
[2]Miller Institute for Basic Research in Science, University of California, Berkeley, CA 94720, USA.
[3]Chemical Sciences Division, Lawrence Berkeley National Laboratory, Berkeley, CA 94720, USA.
[4]Department of Materials Science and Engineering, University of California, Berkeley, CA 94720, USA.
[5]Kavli Energy NanoScience Institute, Berkeley, CA 94720, USA.
[6]Department of Chemistry and Chemical Biology, Cornell University, Ithaca, NY 14853, USA.
[7]Cornell High Energy Synchrotron Source, Cornell University, Ithaca, NY 14853, USA.
[8]School of Applied and Engineering Physics, Cornell University, Ithaca, NY 14853, USA.
[9]Advanced Light Source, Lawrence Berkeley National Laboratory, Berkeley, CA 94720, USA.
[10]Kavli Institute at Cornell for Nanoscale Science, Cornell University, Ithaca, NY 14853, USA.
*Corresponding author: p_yang@berkeley.edu

[11]Y.Y., S.L. and S.Y. contributed equally to this work.

This PDF file includes:

Experimental Details.

Synthesis of 5 nm Cu NPs. 10 mL of trioctylamine (TOA) was purged with N_2 at 130 ^oC for 30 min. After cooling to room temperature, Cu(I) acetate (1 mmol) and TDPA (0.5 mmol) were added while vigorously stirring. The solution was then heated at 180°C for 30 min under N_2. The collected light brown solid (Cu-TDPA complex) was washed with hexane and centrifuged at 5000 rpm for 15 min (25 mL) and repeated twice (10 mL) to remove TOA. A new solution of 10 mL of TOA was purged with N_2 at 130 ^oC for 30 minutes. The orange precipitate was redissolved in 2 mL of 1-octadecene and injected at 250 °C into the solution of TOA (10mL) and reacted for 30 min. The solution was washed and stored following the same procedure used for the 7, 10, and 18 nm NPs. NP concentrations by mass of copper were measured by inductively coupled plasma optical emission spectroscopy. X-ray diffraction (XRD) patterns were acquired on X-ray diffractometer (Bruker D8). Standard XRD patterns and d-spacings of Cu and Cu_2O can be found from in the ICSD database using code numbers of #7954 and #63281, respectively.

Electrochemical measurements in Gas diffusion electrode

Gas diffusion electrode (GDE) (Sigracet, 39 BC) with an active geometric area of 0.3 cm^2 was used in 1 M $KHCO_3$. The flow rate of CO_2 was set to 40 sccm. The cathode and anode were separated by an anion exchange membrane (Selemion, AMV). Cu NP ensemble with a loading of 100 $\mu g/cm^2$ was deposited on the microporous layer (MPL) of a GDE as a working electrode (WE). Platinum gauze was used as a counter electrode while Ag/AgCl (3 M KCl) as a reference electrode. Additional experimental details of flow cell measurements can be found in our early report.[42]

***Operando* EC-STEM measurements**. The electrochemical chip encapsulates a liquid pocket (~500 nm) within two electron-transparent SiN_x windows, which can withstand the ultrahigh vacuum (10^{-8} Torr) inside the TEM chamber. A 2 µL of 0.1 mg/mL Cu NPs solution was drop cast on the microchip and dried to evaporate residual hexane in a vacuum pump. To demonstrate that *operando/in situ* EC-STEM is capable of delivering reliable electrochemical measurements, we performed cyclic voltammetry (CV) measurements of a bulk Pt WE in 0.1 M $HClO_4$ and nanoparticles supported on a carbon WE in CO_2-saturated 0.1 M $KHCO_3$ (Supplementary Fig. 11). The geometry of the three-electrode system is shown in Supplementary Fig. 11a with both RE and CE made of Pt for its chemical stability. The distance between the RE and the WE is small to minimize the iR-drop in a sub-µm-thick electrolyte while the CE has a large surface area to enable rapid polarization. Stage control of EC-STEM holder can record the position of a certain region of interest (ROI) with sub-µm precision. Once the same ROI is identified, STEM videos are acquired at higher magnifications by tracking a particular "marker" at the nm scale, which only undergoes mild or no change after applying electrochemical bias. Such a strategy was used to track movement in STEM video as shown in the identical-location STEM snapshots of 7 nm NPs in Figs. 1c-e as well as the STEM videos of 10 and 18 nm NPs in Supplementary Figs. 25 and 28.

***Operando* HERFD XAS measurements.**

Carbon paper was tailored into 1×5 cm^2 pieces as the catalyst support. The Cu NP catalysts was drop cast on both sides of one end of the carbon paper (1×1 cm^2) and the rest, 1×4 cm^2, served as a non-active conductor with negligible effects on the catalytic current, compared with the active Cu nanocatalysts. A carbon rod used as the counter electrode (CE) was placed 3 cm away from the WE to avoid possible interference of electrochemical reactions on the WE. The electrochemical cell consists of two pieces of chemically inert polyether ether ketone (PEEK) with an X-ray window in the middle (diameter = 1 cm) (Supplementary Fig. 31). One side of the PEEK has a shallow opening to maximize the collection of inherently weak HERFD signals only from the Cu $K\alpha_1$ emission line. A Teflon U-shaped sealing ring was placed between the two PEEK pieces to adjust the electrolyte thickness to less than 200 μm. On top of the electrochemical cell, a PEEK cap with one gas inlet and one gas outlet was used to flow CO_2 gas in 0.1 M $KHCO_3$. All three electrodes were connected to a potentiostat (Biologic SP-200) during *operando* X-ray data acquisition. Cu K-edge was calibrated based on the characteristic absorption edge of Cu metal foil at 8979.0 eV. Fourier transformed EXAFS spectra were plotted by applying a Hanning window from 3 to 10 $Å^{-1}$ with k^2-weighting and no phase correction.

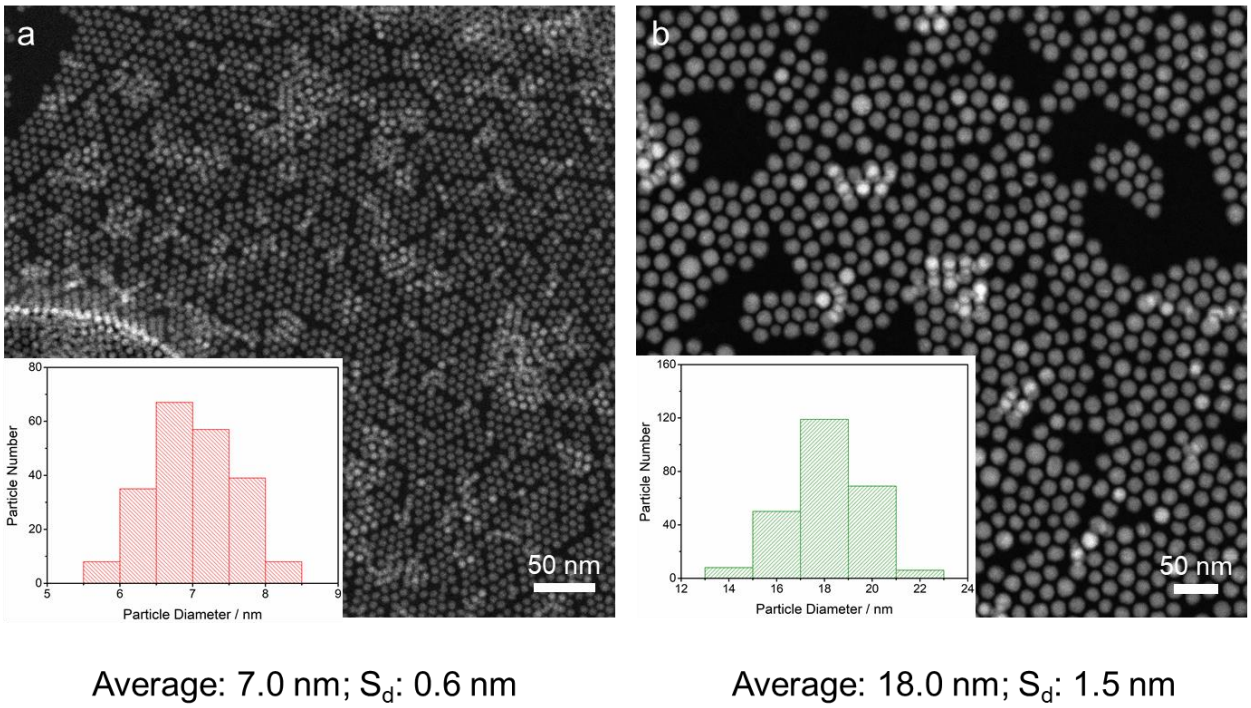

Supplementary Fig. 1. (a-b) HAADF-STEM images of monodisperse 7 and 18 nm NP ensembles. Insets show the particle size distribution histogram of ~500 particles. S_d means one standard deviation.

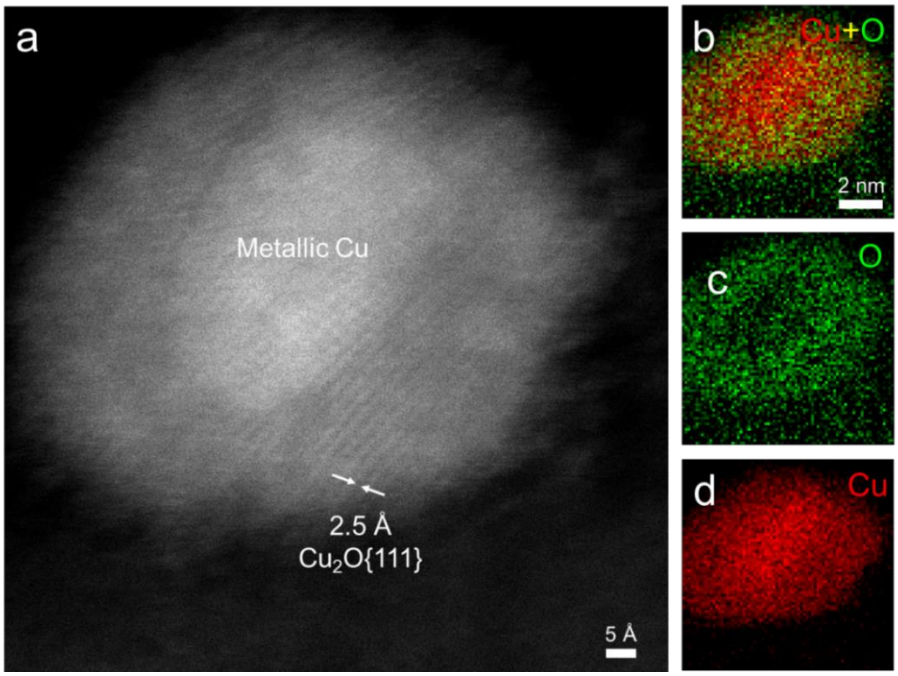

Supplementary Fig. 2. (a) Atomic-scale STEM image of fresh 7 nm NPs (b-d) Corresponding EELS maps of Cu (red) and O (green). Composite map in (b) shows the presence of metallic Cu surrounded by ~2 nm oxide shell.

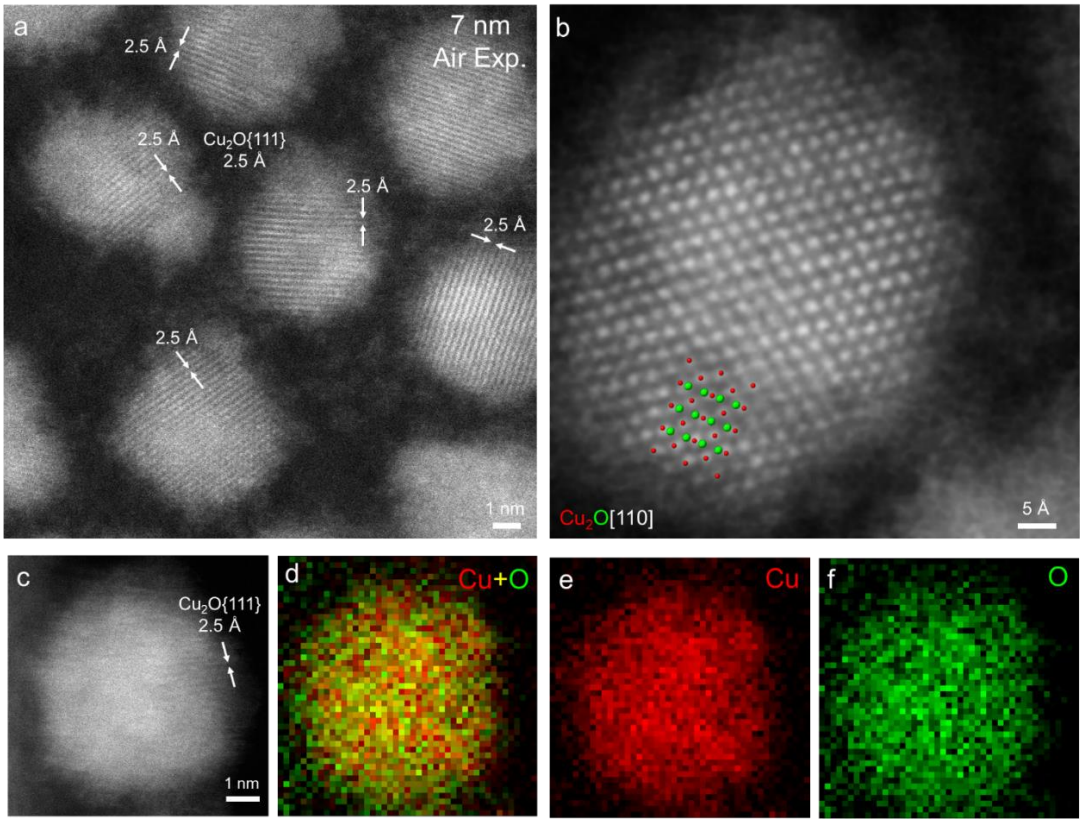

Supplementary Fig. 3. (a) Atomic-scale HAADF-STEM image of 7 nm NPs after air exposure (~5 h) showing single-crystal-type Cu_2O{111} d-spacings (2.5 Å). (b) Atomic-scale STEM image of a fully oxidized 7 nm NPs with the single-crystal Cu_2O structure that matches well with the crystal model of Cu_2O[110] zone axis (Cu and O atoms in red and green, respectively). STEM images were processed using Gaussian denoising with Sigma(Radius) of 2 using ImageJ software. Those STEM images are consistent with the oxidation from 7 nm Cu@Cu_2O NPs to Cu_2O NPs after more than 5 h air exposure based on XRD patterns (Supplementary Fig. 4). (b-e) STEM image of 7 nm NPs and corresponding EELS elemental maps of Cu (red) and O (green). Composite map in (d) exhibits the homogenous elemental distribution of Cu and O.

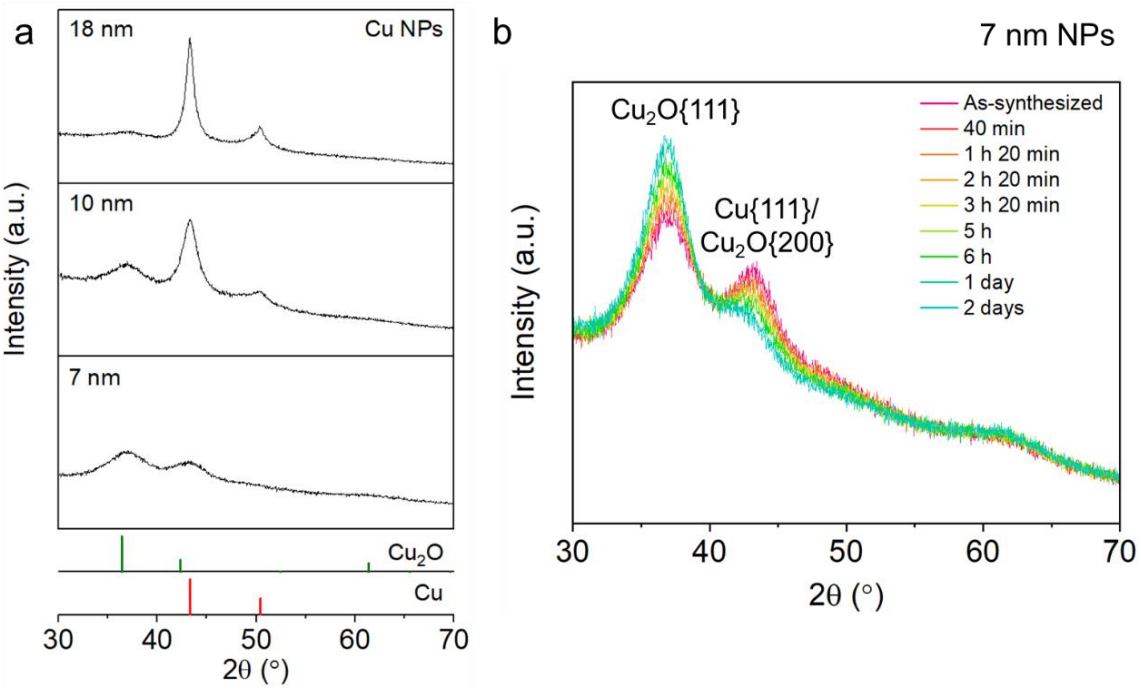

Supplementary Fig. 4. (a) XRD patterns of as-synthesized 7, 10, and 18 nm NPs are consistent with the presence of Cu@Cu_2O core-shell structures. (b) XRD patterns of 7 nm NPs showing Cu@Cu_2O structure right after synthesis (Day 0), which evolved into Cu_2O NPs after air exposure for about 5 h and remained at the same level of oxidation after longer air exposure (1-2 days).

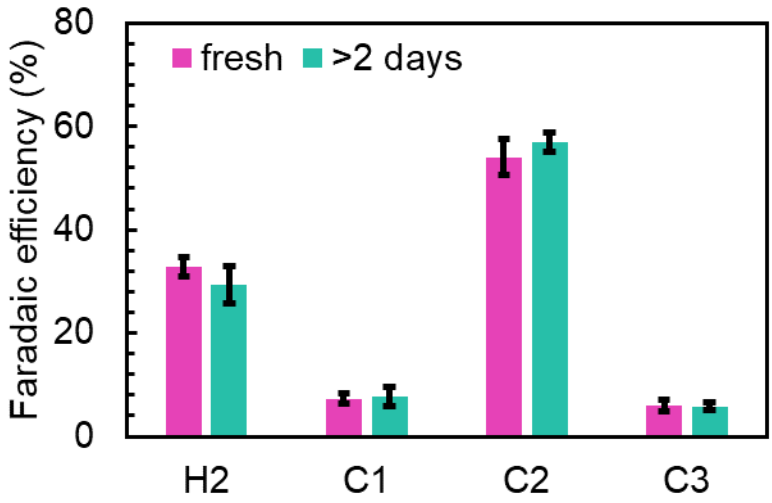

Supplementary Fig. 5. Similar CO_2RR activities were achieved for fresh 7 nm Cu@Cu_2O core-shell nanoparticles and 7 nm fully oxidized Cu_2O NPs after an extended period time of air exposure (>2 days).

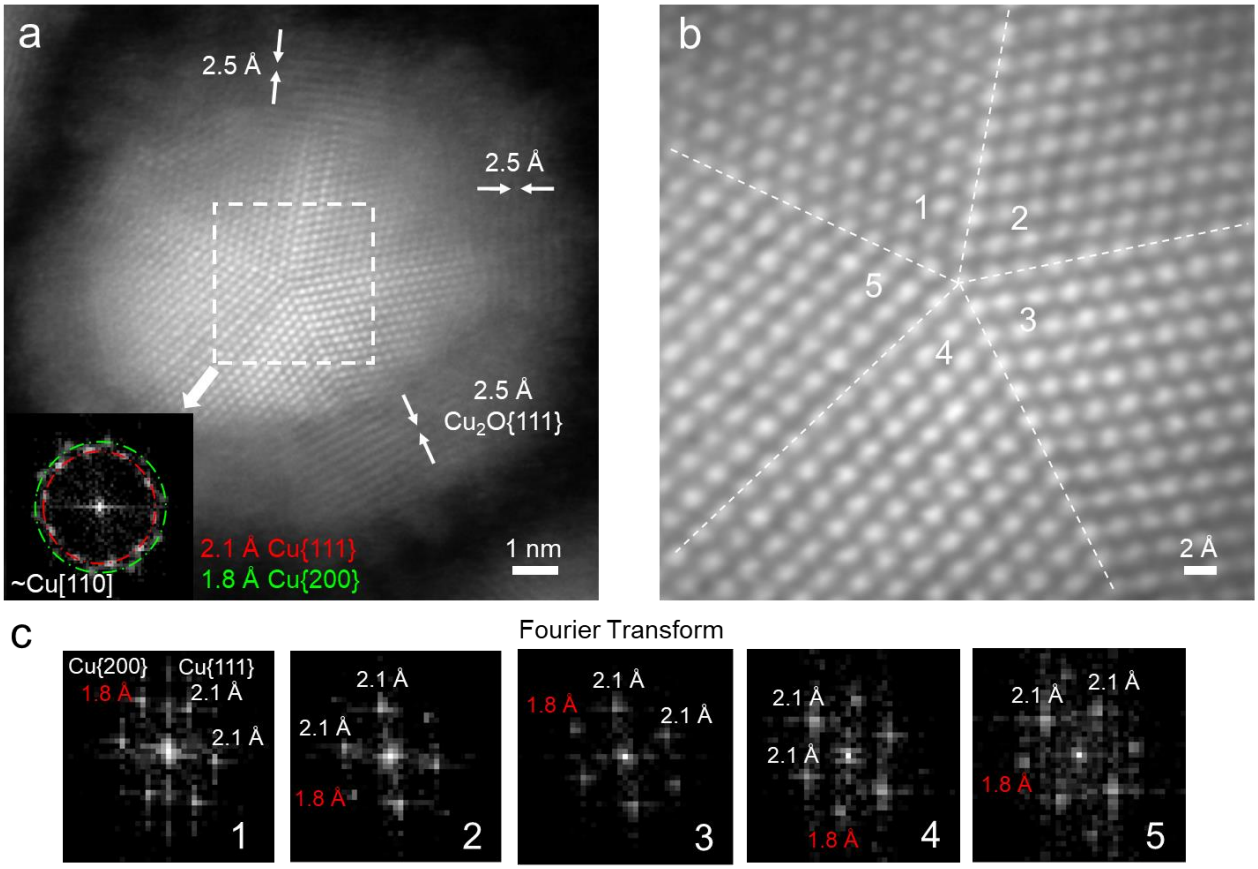

Supplementary Fig. 6. (a) Atomic-scale STEM image of 10 nm Cu@Cu_2O NPs with five metallic Cu domains in the core and Cu_2O in the shell as indexed by the Cu_2O{111} (2.5 Å). Inset shows the diffraction rings of Cu{111} (1.8 Å) and Cu{200} (2.1 Å). (b-c) Enlarged STEM image

showing five Cu domains with domain boundaries marked by the dashed line, and the corresponding Fourier transform patterns showing the diffraction spots of Cu{111} and Cu{200} close to the Cu[110] zone axis.

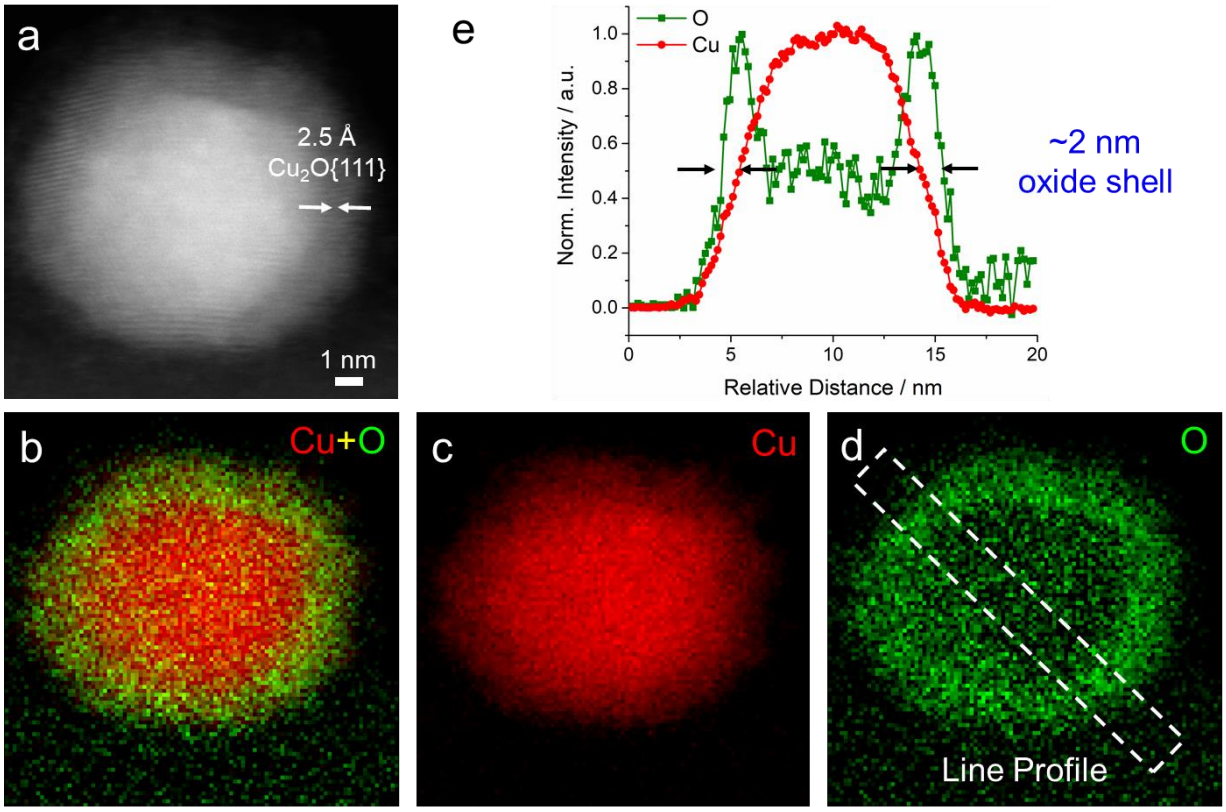

Supplementary Fig. 7. STEM image of 10 nm NPs (a) and corresponding EELS elemental maps of Cu and O (b-d) showing the Cu@Cu_2O core-shell structures. The EELS line profile in (e) extracted from the dashed box in (d) shows an average oxide shell thickness of around 2 nm.

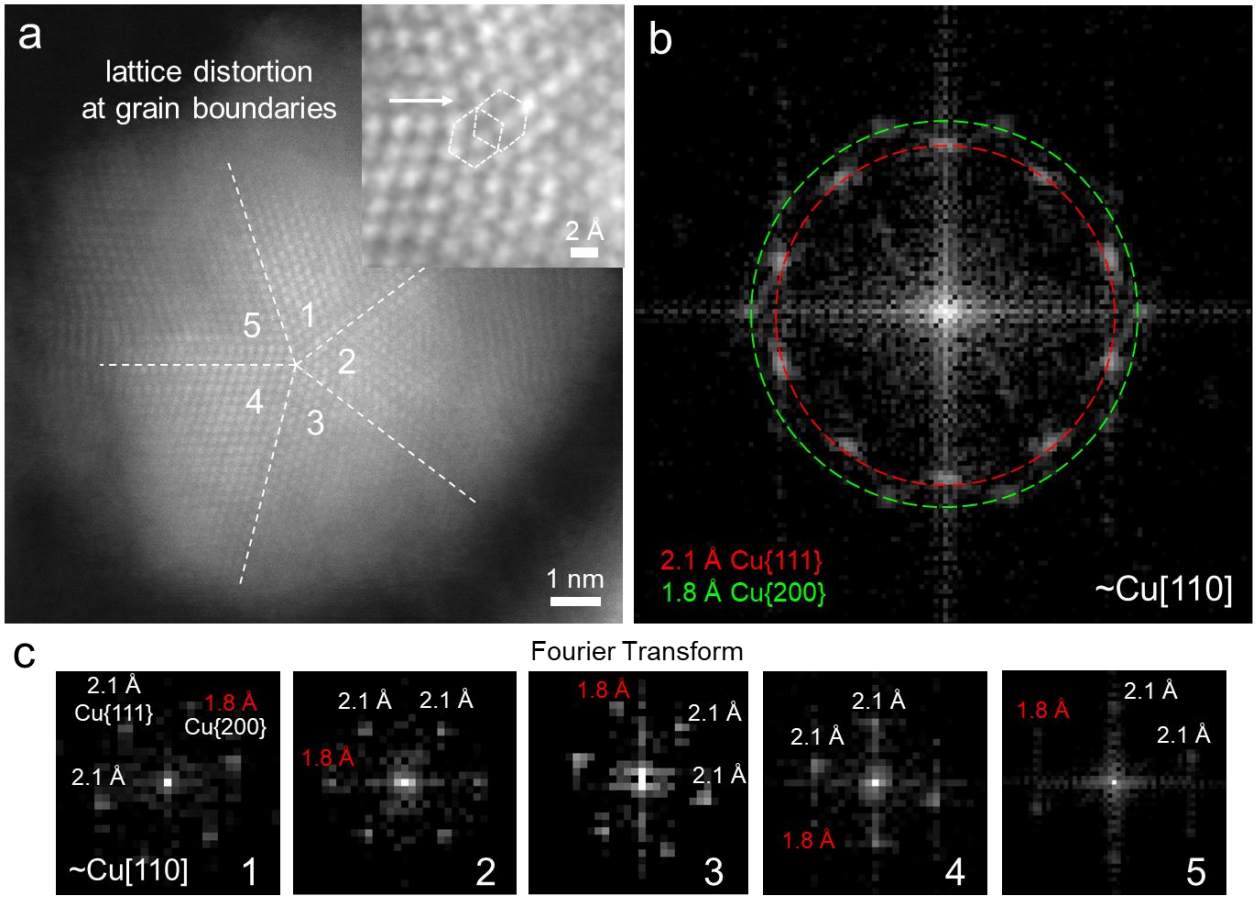

Supplementary Fig. 8. (a) Atomic-scale STEM image of 18 nm NPs with five metallic Cu domains in the core and Cu_2O in the shell as indexed by the Cu_2O{111} (2.5 Å). Inset shows the lattice distortion at the grain boundaries among the five Cu domains. (b) Diffraction rings of Cu{111} (1.8 Å) and Cu{200} (2.1 Å) extracted from the metallic Cu in (a) close to the Cu[110] zone axis. (c) The Fourier transform patterns, corresponding to the 1-5 domains in (a), show the diffraction spots of Cu{111} and Cu{200}.

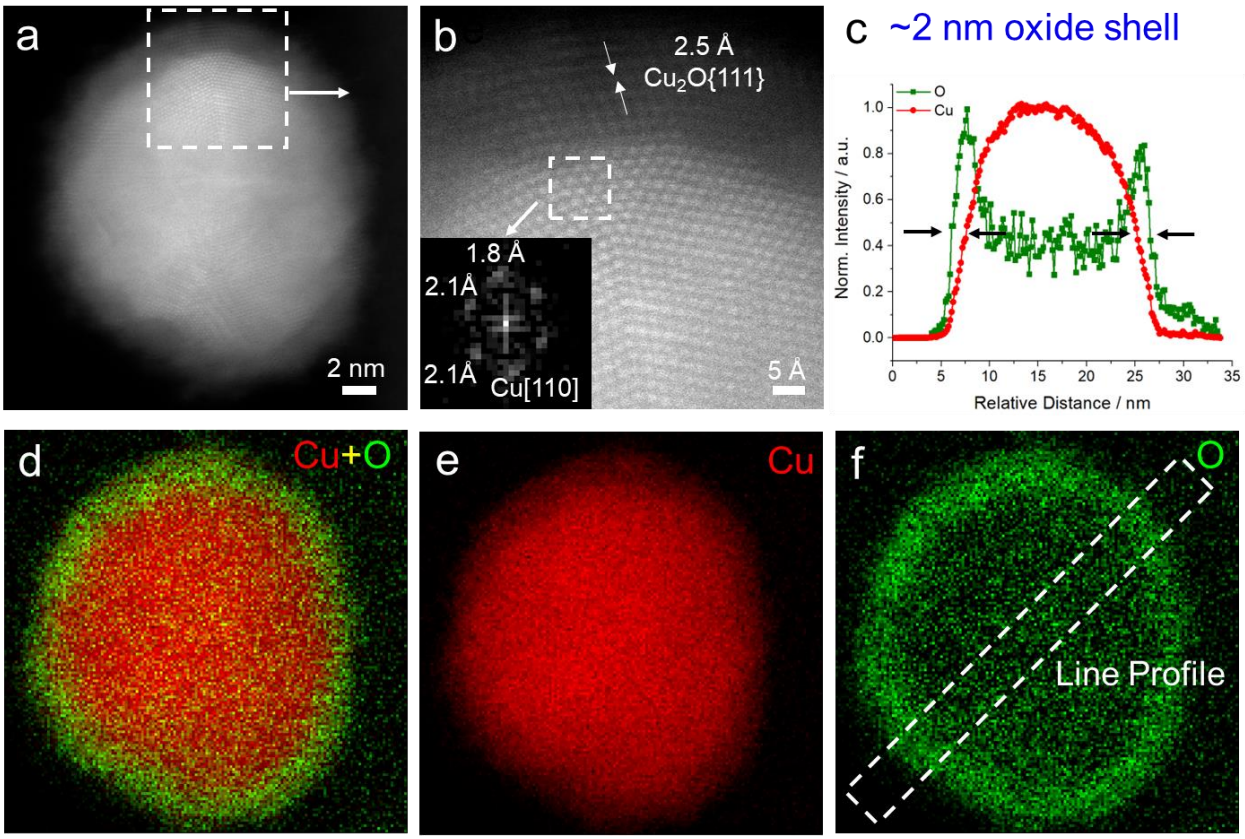

Supplementary Fig. 9. STEM image of 18 nm NPs (a-b) and corresponding EELS elemental maps of Cu and O (d-f) showing the Cu@Cu_2O core-shell structures. The EELS line profile in (c) extracted from the dashed box in (f) shows an average oxide shell thickness of about 2 nm.

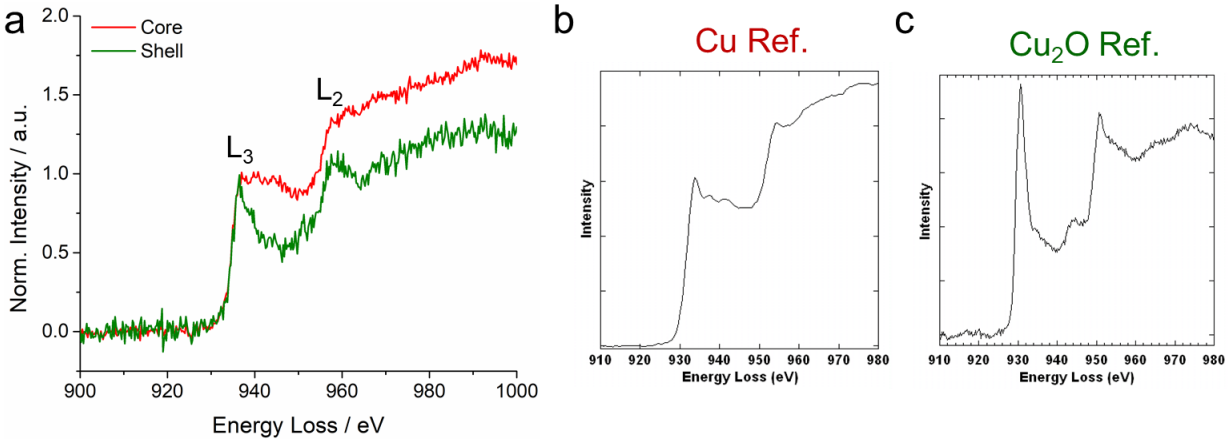

Supplementary Fig. 10. EELS spectra show the fine electronic structures of the 18 nm Cu@Cu_2O NP in Supplementary Fig. 9. Metallic Cu core shows the delayed L_2 edge due to the fully occupied d orbitals while Cu_2O shell shows the pronounced L_2 peaks at ~960 eV. They are consistent with the standard EELS references of Cu foil and bulk Cu_2O. (https://muller.research.engineering.cornell.edu/web-eels/).

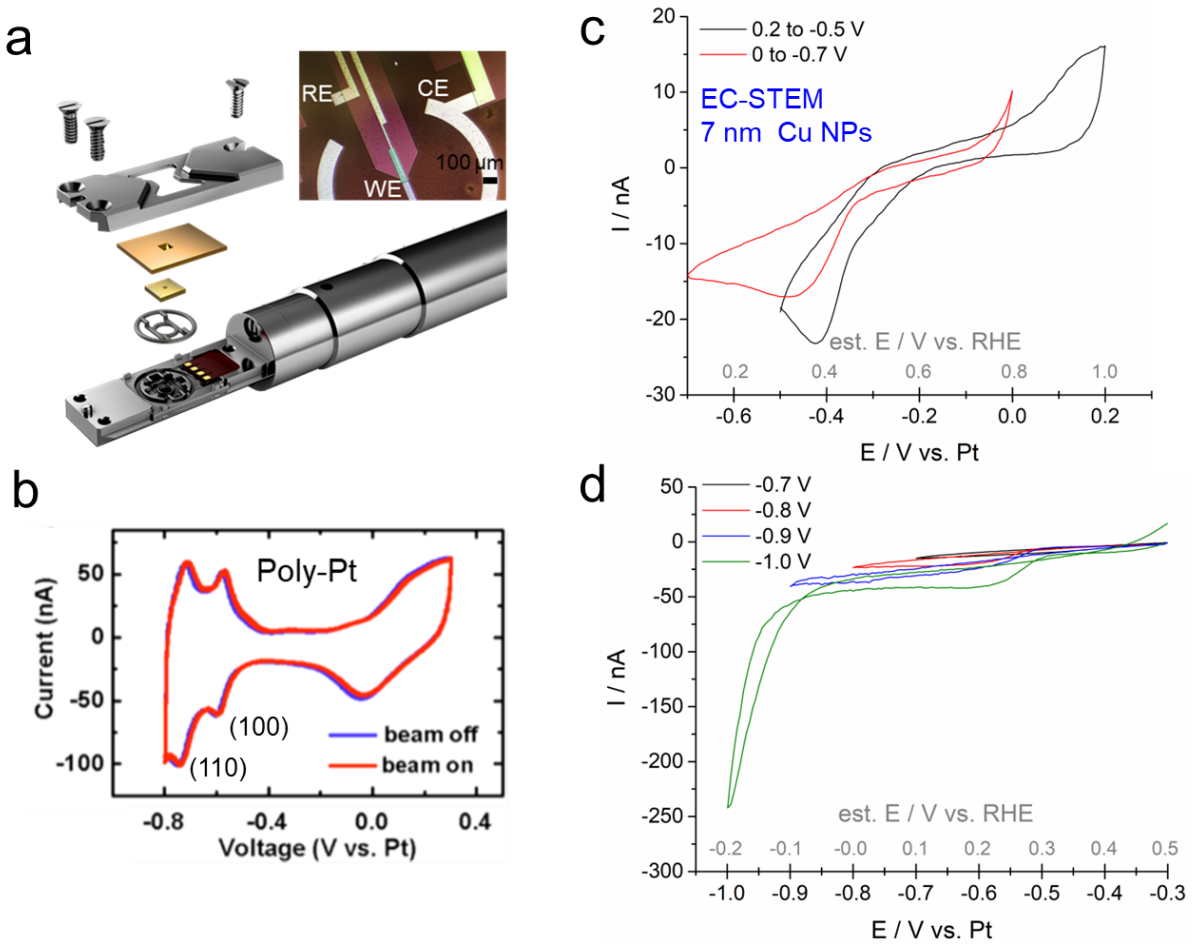

Supplementary Fig. 11. (a) Schematic of the layered structure of a Protochips Poseidon liquid-cell holder. Inset: optical image of the three-electrode microchip loaded with nanoparticles. (b) CV profiles of polycrystalline Pt films in 0.1 M $HClO_4$ when the electron beam is on and off from our previous study[27]. Negligible changes in CV profiles were detected when the electron beam was turned on, indicating negligible beam-induced effects on electrochemical measurements. Those CV profiles showed the characteristic behavior of poly-Pt with two pairs of hydrogen adsorption/desorption peaks ({110} facets at -0.75 V and {100} facets at -0.6 V vs. Pt) as well as the broad Pt oxidation/reduction peaks. Given that the position of the characteristic Pt{110} is often located at ~0.1 V vs. RHE, we estimate the potential of the Pt pseudo-RE to be 0.8 $\pm$ 0.1 V higher than that of the SHE in 0.1 M acid. Given the potential of Pt pseudo-RE has the same/similar Nernstian pH-dependence as the RHE, the difference between Pt pseudo-RE and RHE was also estimated to be 0.8 $\pm$ 0.1 V. A more rigorous calibration of Pt pseudo-RE is under current investigation. (c-d) CV profiles of 7 nm NPs at 100 mV/s in CO_2-sat. 0.1 $KHCO_3$ with a well-defined reduction peak at ~0.4 V vs. RHE, which matches well with results from a standard electrochemical cell as shown in Supplementary Fig. 32b. Cathodic current density increased progressively as applied potentials became more negative and approached the CO_2 reduction relevant conditions.

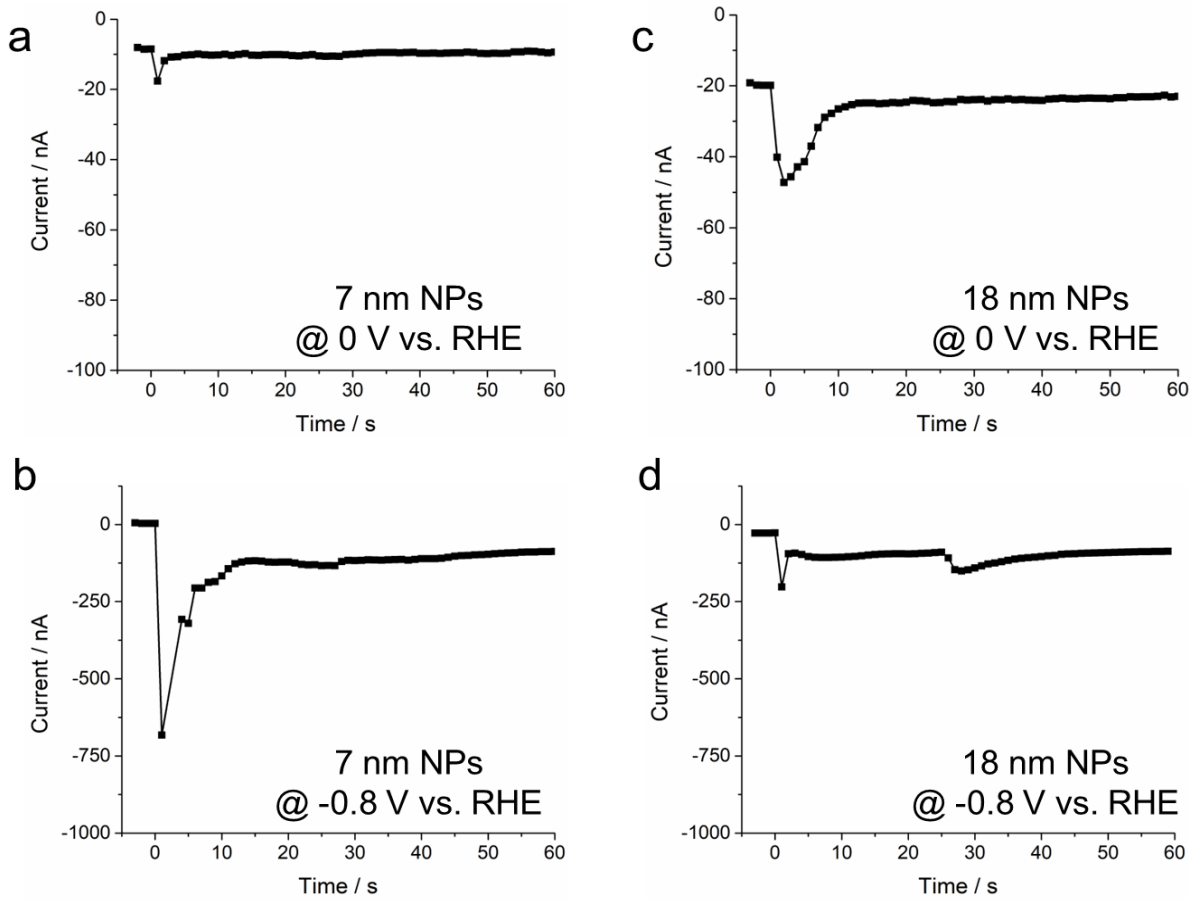

Supplementary Fig. 12. Chronoamperometry (CA) profiles of 7 nm NPs (a-b) and 18 nm NPs (c-d) at 0 and -0.8 V vs. RHE, showing stable current plateaus during *operando* EC-STEM measurements. 7 and 18 nm NPs show comparable faradaic current of around -100 nA at -0.8 V vs. RHE. Given the geometric area of glassy carbon microelectrode (2500 μm^2) in a liquid cell, 7 nm NPs show a geometric current density of about -4 mA/cm^2 at -0.8 V vs. RHE in EC-STEM measurements. Given the difference in the conductive supports used for thin-liquid EC-STEM cell (glassy carbon electrode) and standard H-cell (porous carbon paper), it is well within the similar order of magnitude (-4 vs. -14 mA/cm^2, respectively) (Supplementary Fig. 13). In addition, 7 nm NPs show a slightly lower hydrogen evolution reaction (HER) current of -11 nA at 0 V vs. RHE than that of 18 nm NPs (-24 nA), which is consistent with the lower H_2 faradaic efficiency of 7 nm NPs as measured by GC in H-cell setup.

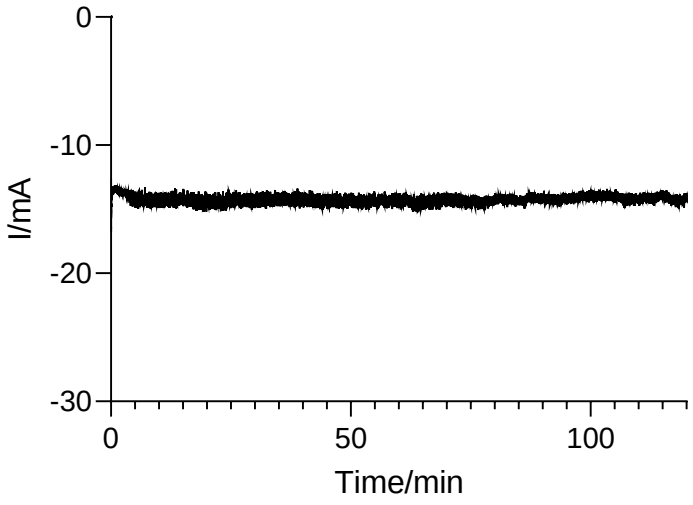

Supplementary Fig. 13. Stable current density of the 7 nm NP ensemble at -0.8 V vs. RHE measured in an H-cell configuration.

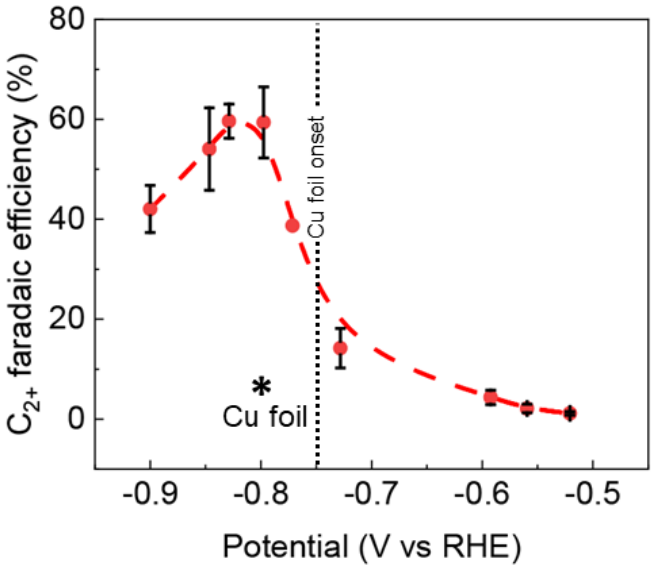

Supplementary Fig. 14. C_{2+} faradaic efficiency of the 7 nm Cu NP ensemble at various applied potentials in CO_2-sat. 0.1 M $KHCO_3$. The C_{2+} onset potential and C_{2+} FE of Cu foil at -0.8 V vs RHE are annotated by a black dashed line and a black asterisk, respectively. This figure indicates the stark contrast in C_{2+} activity between the benchmark Cu foil and the 7 nm Cu NP ensemble at -0.80 vs RHE where the latter reaches its peak C_{2+} activity. Moreover, the onset potential for C_{2+} formation on the 7 nm Cu NP ensemble is only -0.57 V vs. RHE, which is 180 mV lower compared to Cu foil at -0.75 V vs. RHE. The potential-dependent CO_2RR of the 7 nm Cu NP ensemble towards C_{2+} products clearly identifies -0.8 V vs RHE as the optimal potential for C-C coupling which was thus selected as the most C_{2+} relevant potential for our subsequent *operando* characterizations.

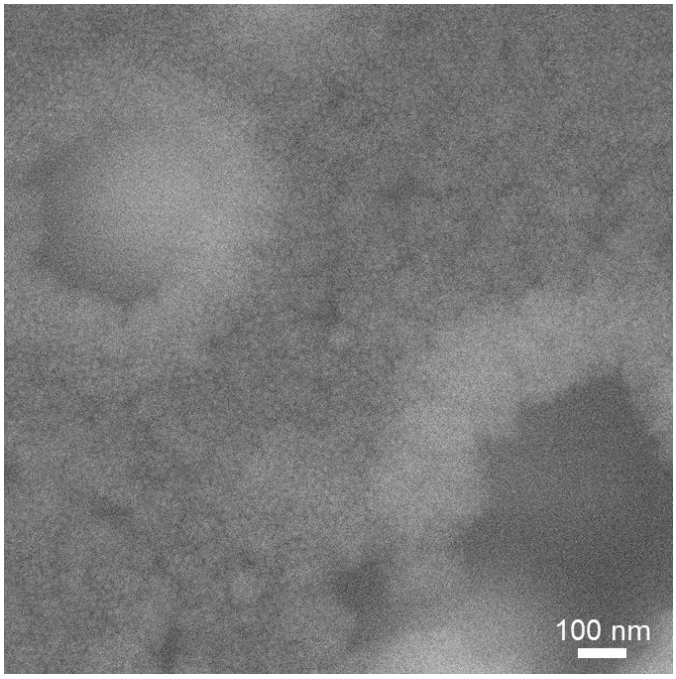

Supplementary Fig. 15. Static liquid-cell STEM image of 18 nm in ~500 nm thick electrolyte. In comparison, 7 nm NPs are not resolvable in such thick liquid and require a voltametric scan from 0.4 to 0 V vs. RHE to induce a hydrogen bubble and enable a thinner liquid layer.

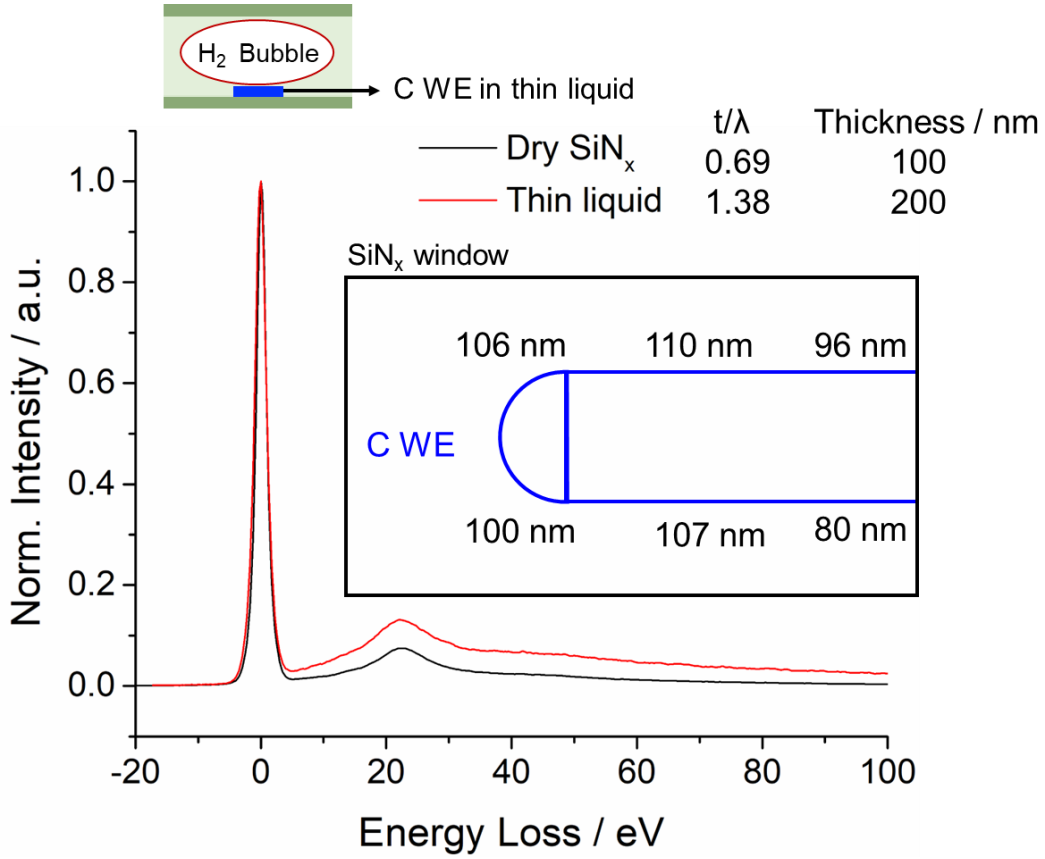

Supplementary Fig. 16. Quantification of the thickness of the thin-liquid film at -0.8 V vs. RHE by EELS measurements. The liquid thickness (t) was estimated using Beer's law ($I = I_0\exp(-t/\lambda)$) in which λ is the inelastic mean free path, I and I_o are the intensity of unscattered electron in the zero-loss peak (ZLP) and the total intensity of incident electron, respectively. λ is 145 nm at 300 keV and a collection angle of 40 mrad on Titan STEM. The intensity of the plasmon peak at around 20 eV, relative to the ZLP, reflects the energy loss due to inelastic scattering. The thickness of the thin-liquid film was estimated to be around 100 nm after subtracting the thickness of the two dry SiN_x windows (~100 nm) from the total thickness of the thin liquid film and windows (~200 nm). The thickness of the thin-liquid film was estimated to be 100 ± 10 nm after averaging measurements at six different locations near the carbon WE (Inset).

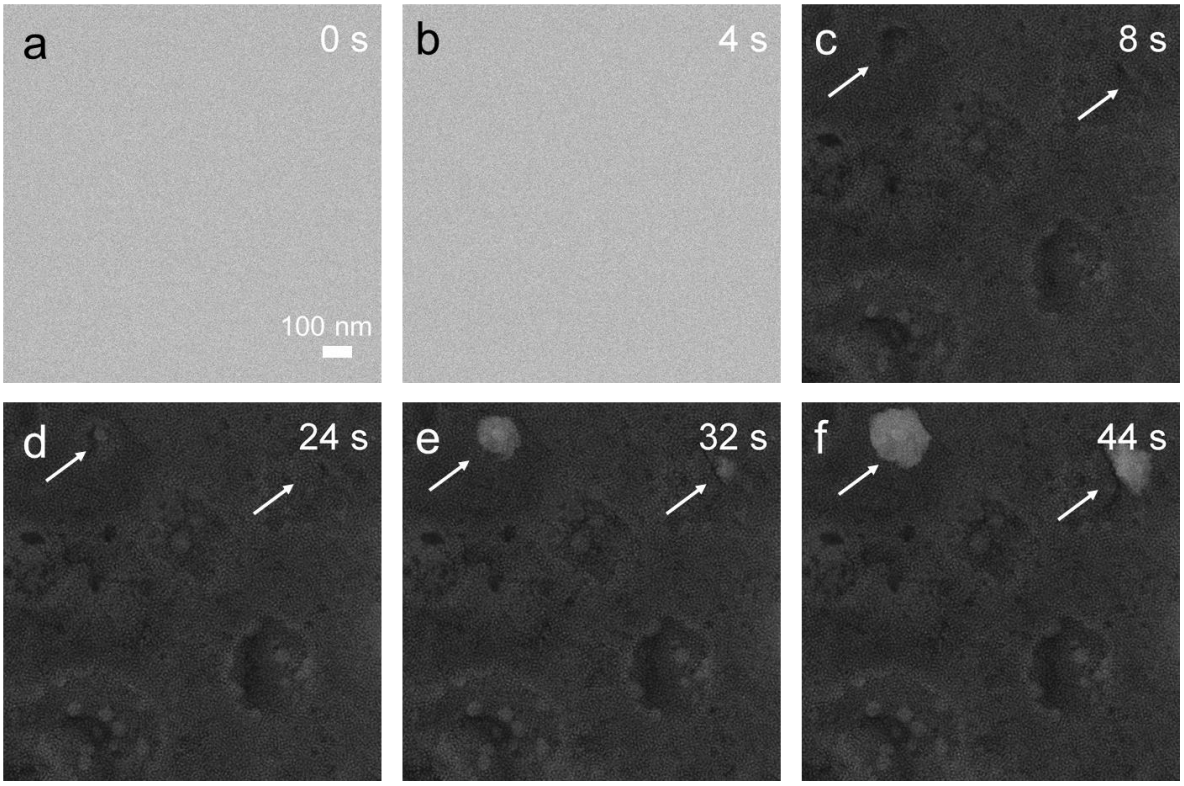

Supplementary Fig. 17. *Operando* EC-STEM images of Cu NPs under cyclic voltammetry (CV) with scanning from 0.4 to 0 V vs. RHE at 100 mV/s in CO_2-sat. 0.1 M $KHCO_3$ (a-f). A H_2 bubble is triggered at 8 s (around 0 V vs. RHE) to create a thin liquid film and significantly enhanced spatial resolution for tracking particle growth as indicated by the arrows.

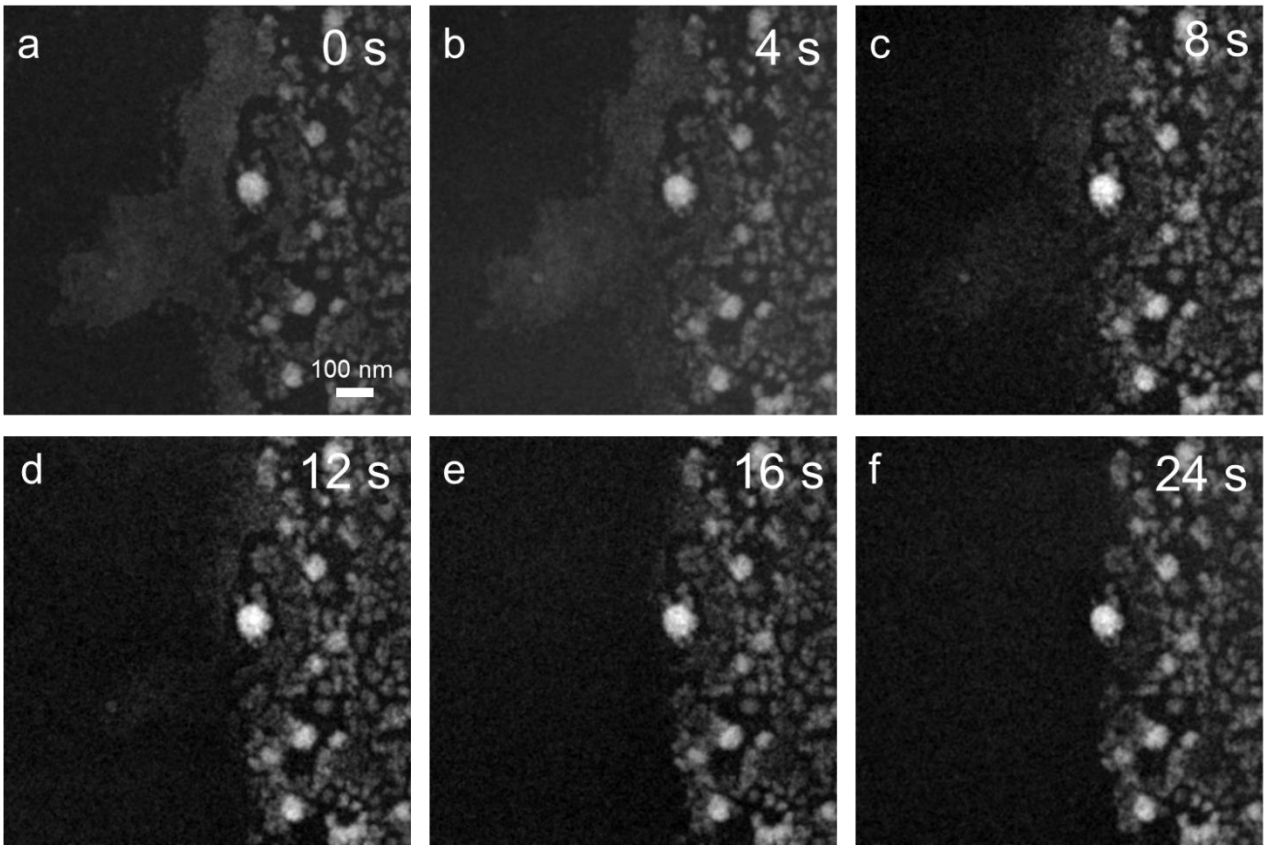

Supplementary Fig. 18. *Operando* EC-STEM images of 7 nm NPs at 0 V vs. RHE in CO_2-sat. 0.1 M $KHCO_3$ over 24 s, corresponding to Figs. 1f-i and Supplementary Video 2.

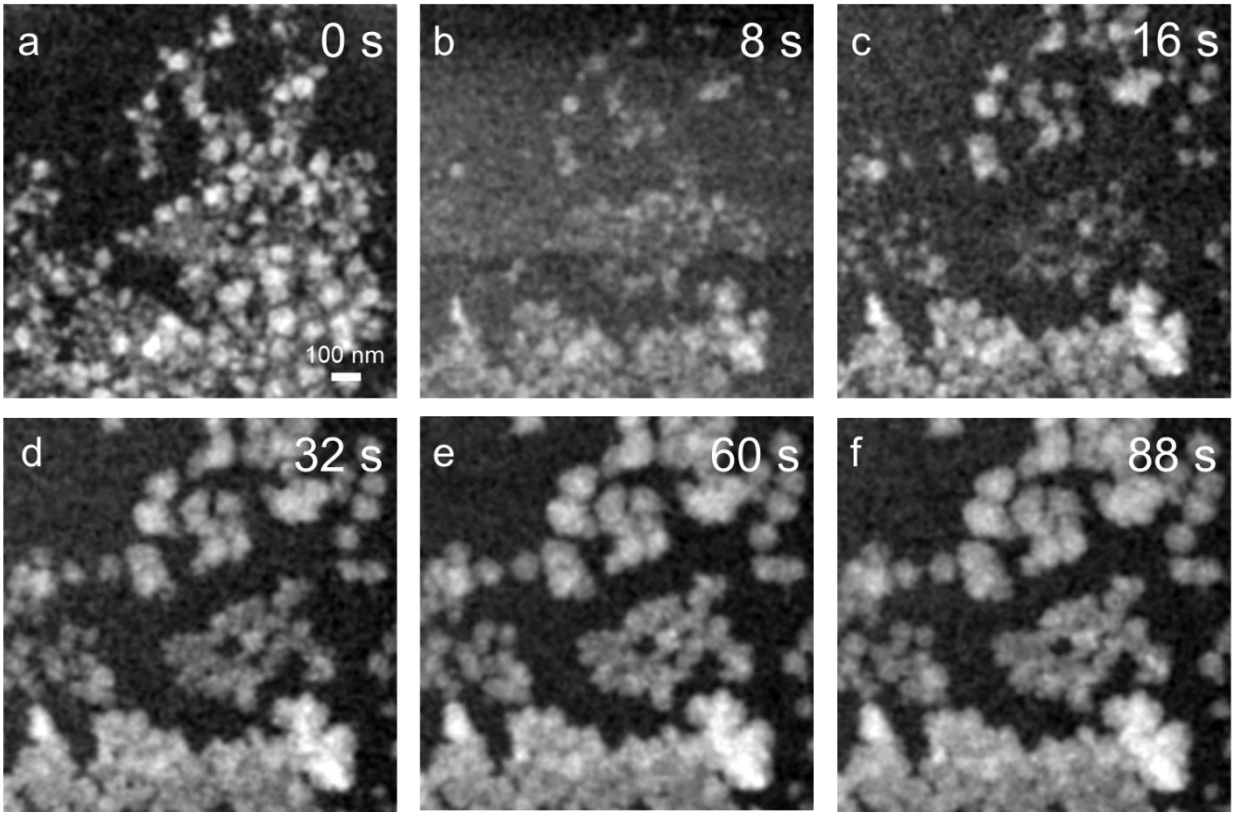

Supplementary Fig. 19. *Operando* EC-STEM images of 7 nm NPs at -0.8 V vs. RHE in CO_2-sat. 0.1 M $KHCO_3$ over an extended time period of 88 s, corresponding to Figs. 1j-m and Supplementary Video 3. We note that the sudden change in the image contrast at 8 s is due to fluctuation in liquid thickness instead of beam-induced artifacts since it is a uniform fluctuation of background intensity through the entire image. Such fluctuation in liquid thickness was only triggered by electrochemical bias, as commonly observed in Supplementary Videos 1, 5 and 6 and Supplementary Fig. 25, in which a 20-40 second counting down was performed before potentials were applied to ensure no beam damage at a low beam dose rate of ~12.5 e^-/nm^2s during the time period of *operando* EC-STEM videos.

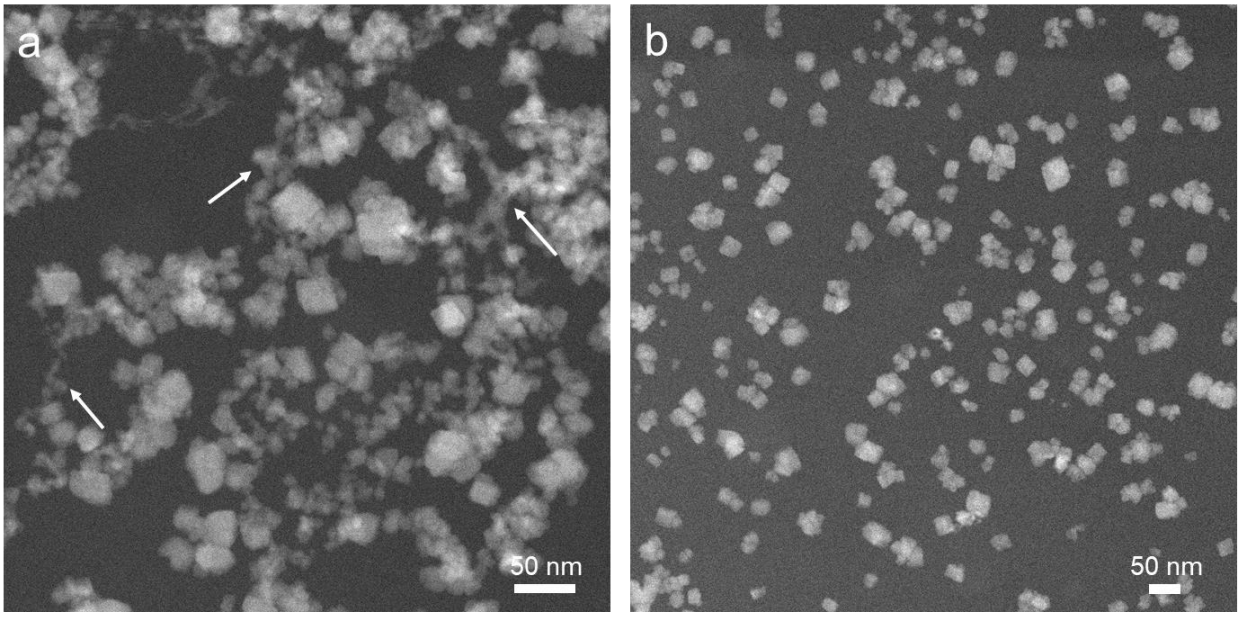

Supplementary Fig. 20. *Ex situ* STEM images from the same EC-STEM setup after air exposure showing either (a) particle chains in the process of form Cu_2O cubes (marked by arrows) or (b) the complete formation of Cu_2O nanocubes.

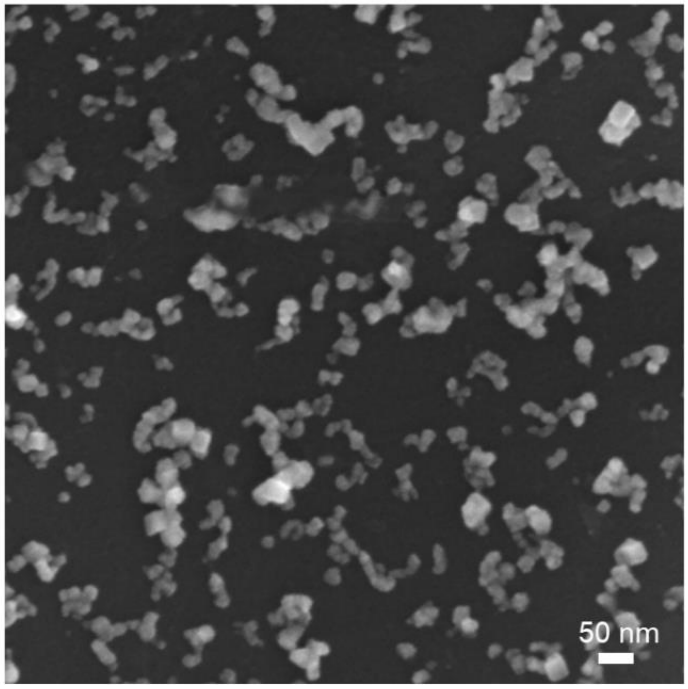

Supplementary Fig. 21. Post-electrolysis Cu_2O nanocubes after H-cell measurements with similar morphology to that in EC-STEM cell in Supplementary Fig. 20b.

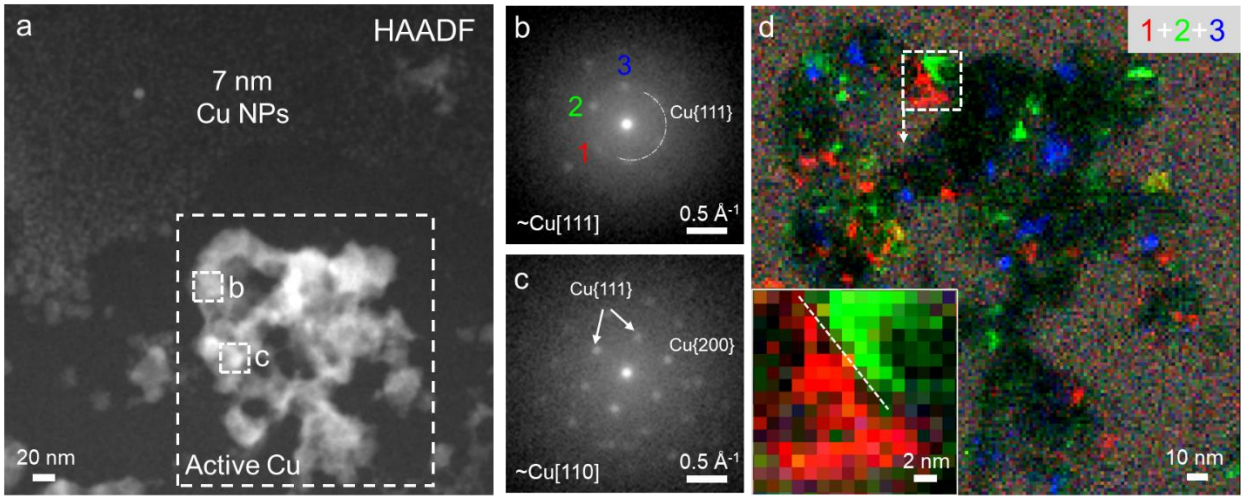

Supplementary Fig. 22. (a) HAADF-STEM images of co-existed 7 nm NPs and active Cu nanograins in loosely connected chains after the initial growth at 0 V vs. RHE. (b-c) Selective examples of electron diffraction patterns of Cu domains from the dashed box in (a), showing fcc metallic Cu features with Cu{111} (2.1 Å) and Cu{200} (1.8 Å) near the [111] (b) or [110] zone axis (c). (d) False-color dark-field 4D-STEM maps showing Cu nanograins with diffraction spots resembling those three marked as 1 (red), 2 (green), and 3 (blue), respectively, in (b). Inset in (d) shows the enlarged region with a nanograin boundary marked by the dashed line.

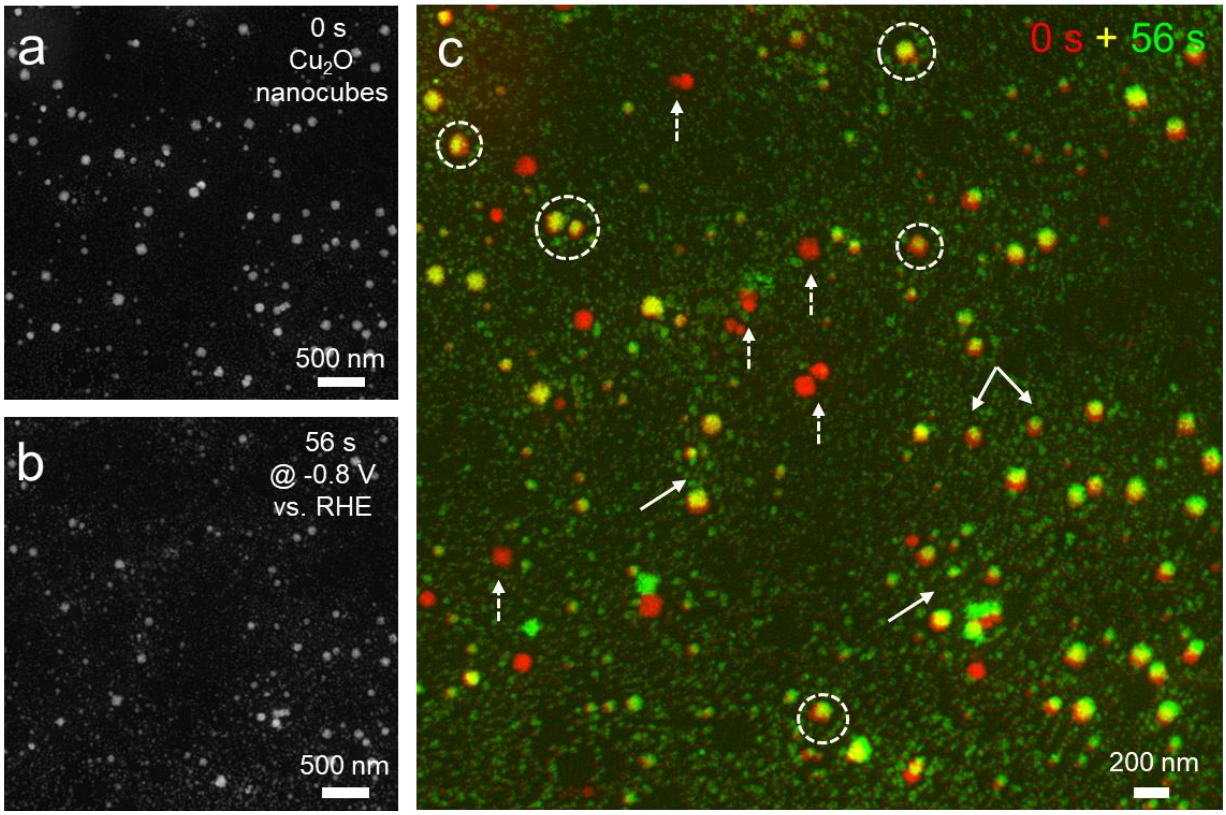

Supplementary Fig. 23. *Operando* EC-STEM images of Cu_2O nanocubes in CO_2-sat. 0.1 M $KHCO_3$. (a) STEM image of Cu_2O nanocubes after a linear sweep voltammetry (LSV) scan from 0.4 to 0 V vs. RHE to trigger a H_2 bubble. (b) STEM image of Cu_2O nanocubes at the same location as (a) after 56 s at -0.8 V vs. RHE. (c) False color overlay of STEM images in (a) and (b). At -0.8 V vs. RHE for about 1 min, Cu_2O nanocubes with a size of ~100 nm experienced fragmentation, decay in sizes and deformation in cubic shapes, as indicated by dashed circles, complete decomposition as indicated by the dashed arrows and redeposition of new nanoclusters with the majority less than 20 nm, as indicated by the solid arrows. Detailed morphological changes of Cu_2O nanocubes from 0 to 56 s can be found in *operando* EC-STEM videos in Supplementary Video 4.

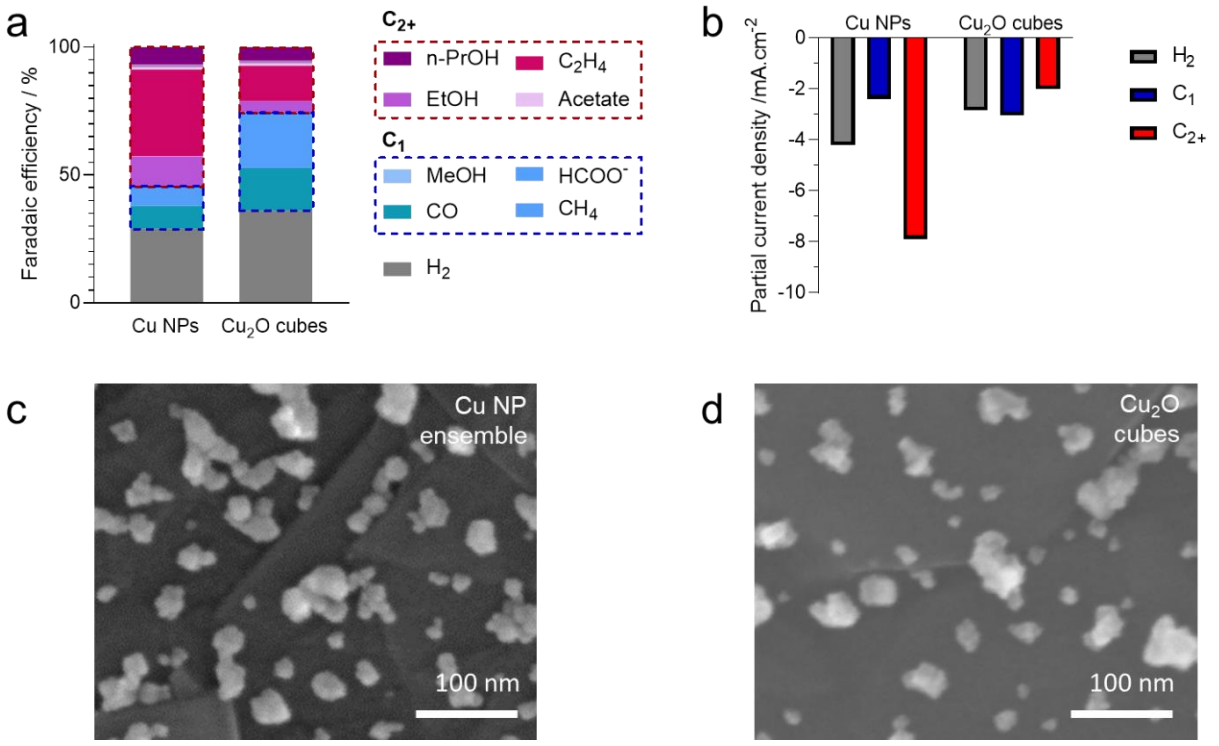

Supplementary Fig. 24. Comparison of the CO_2RR performance of the 7 nm Cu NP ensemble and post-electrolysis Cu_2O nanocubes in (a) faradaic efficiency and (b) partial current density at -0.8 V vs. RHE. Post-electrolysis *ex situ* SEM images of the (c) Cu NP ensemble and (d) the post-electrolysis Cu_2O cubes.

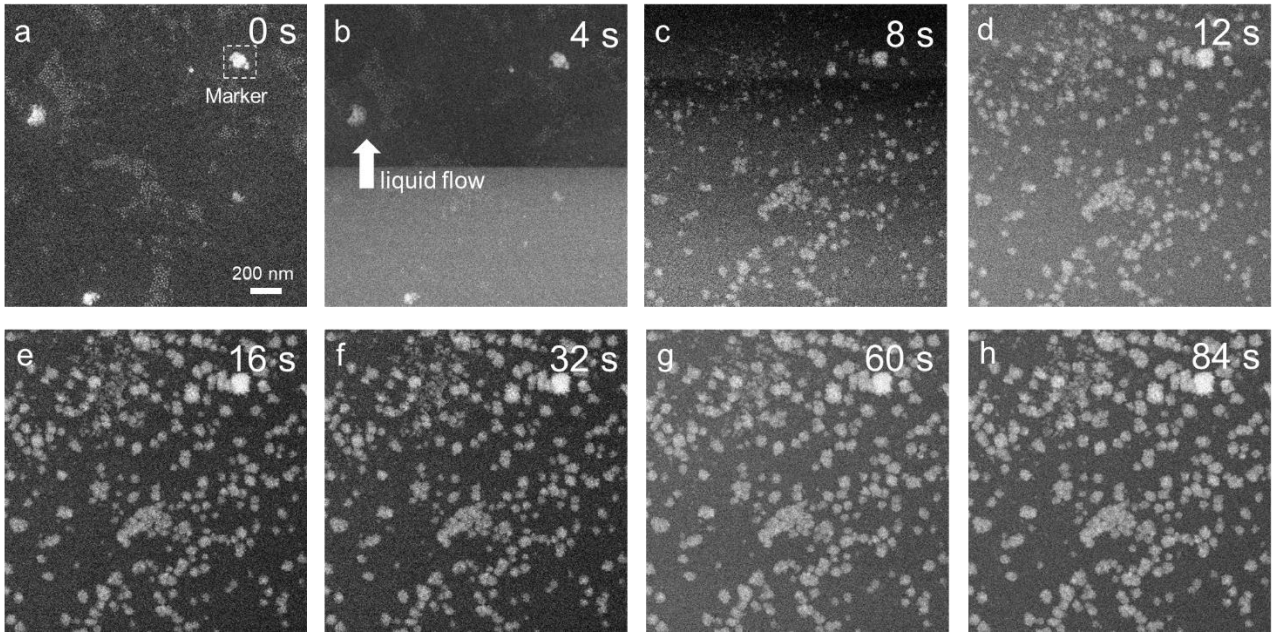

Supplementary Fig. 25. (a-h) *Operando* EC-STEM images of 10 nm NPs at -0.8 V vs. RHE in CO_2-sat. 0.1 M $KHCO_3$ over an extended time period of 1.5 min, corresponding to Figs. 3a-d and Supplementary Video 5. The arrow in (b) indicates the flow of a thick liquid layer over the sample at the beginning of the electroreduction. Most of the morphological changes were complete within the first 32 s and structures of Cu nanograins approached a steady state at 84 s. Given the larger particle size, 10 nm NPs were resolved at a lower magnification than 7 nm NPs and thus required a lower beam dose rate of ~5 e^-/nm^2s.

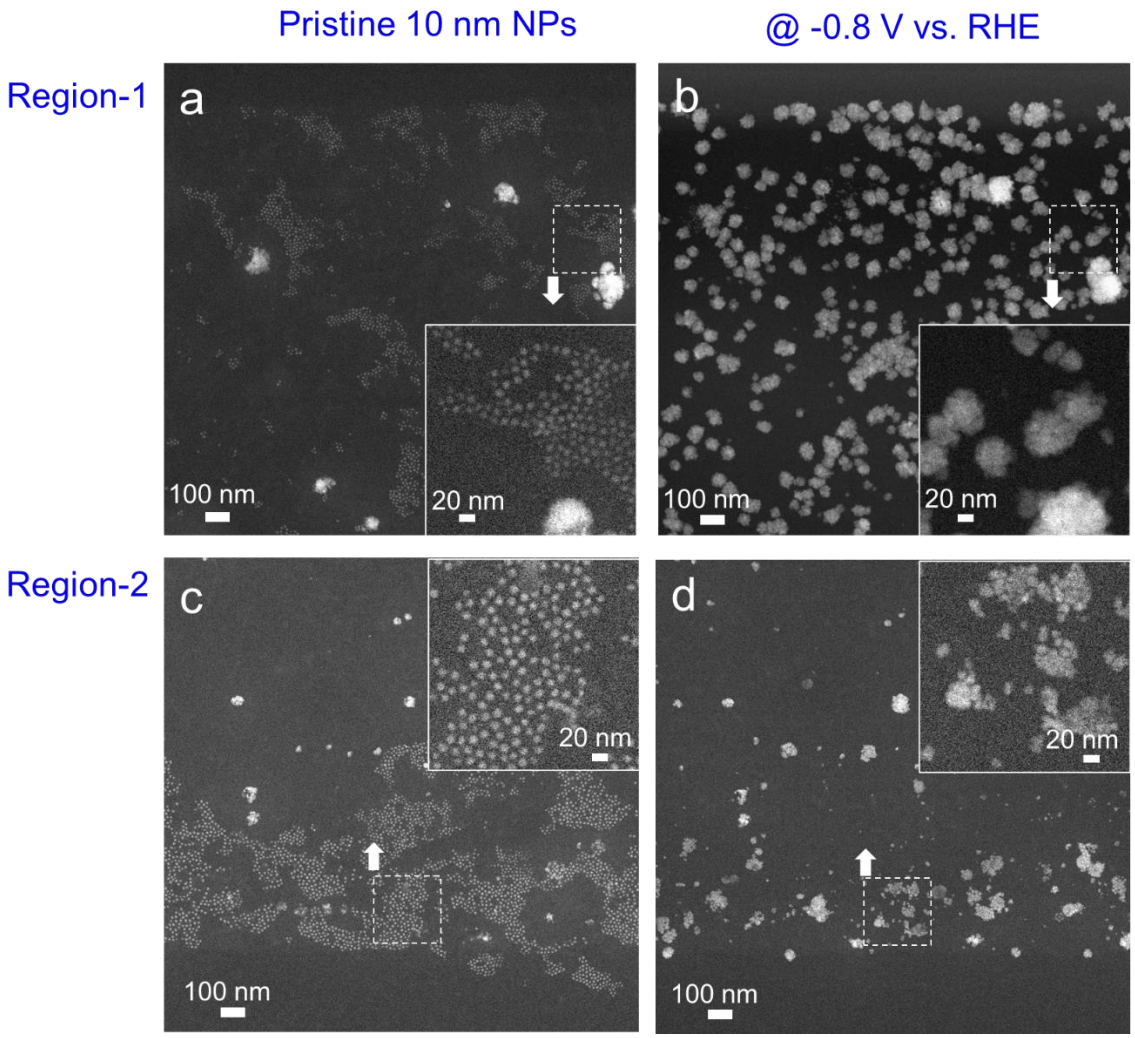

Supplementary Fig. 26. *Operando* EC-STEM images tracking the dynamic evolution of 10 nm NPs at -0.8 V vs. RHE for 90 s in two regions (a-b) and (c-d). The insets in the Region-1 (a-b) shows the formation of closely packed Cu nanograins while the insets in the Region-2 (c-d) shows that some Cu nanograins are rather incomplete and were in the process of packing individual grains.

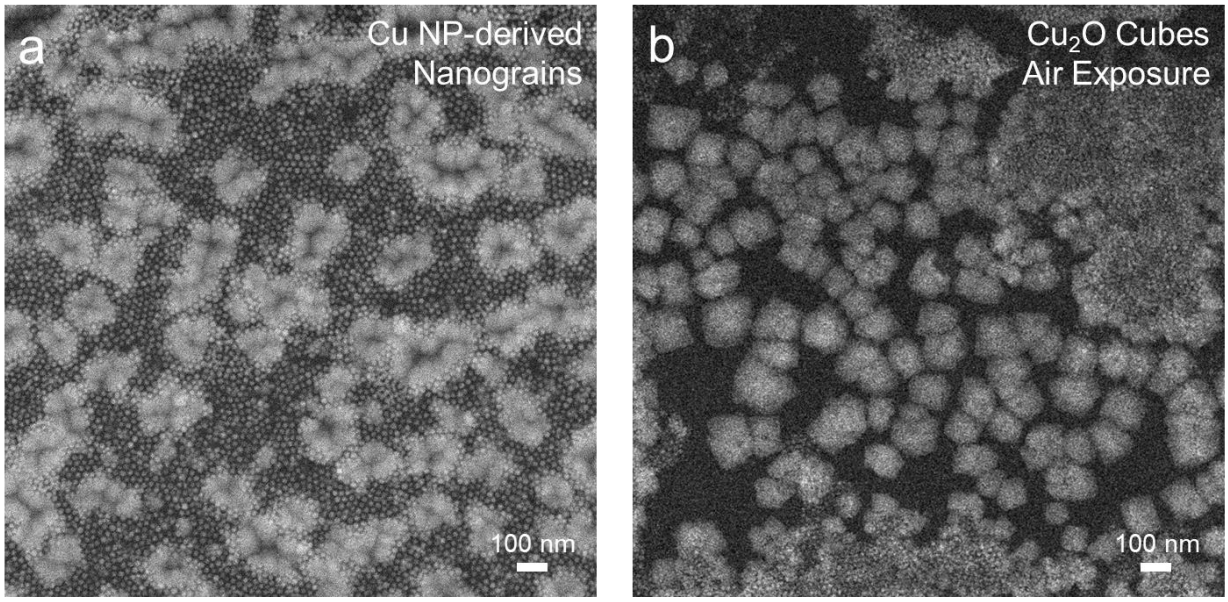

Supplementary Fig. 27. (a) *Operando* EC-STEM image of 18 nm at 0 V vs. RHE showing the "melting" Cu nanograin features. (b) After air exposure, EC-STEM image of 18 nm NPs showing the conversion of the "melting" Cu nanograins to Cu_2O nanocubes with unreacted 18 nm NPs maintaining initial morphology.

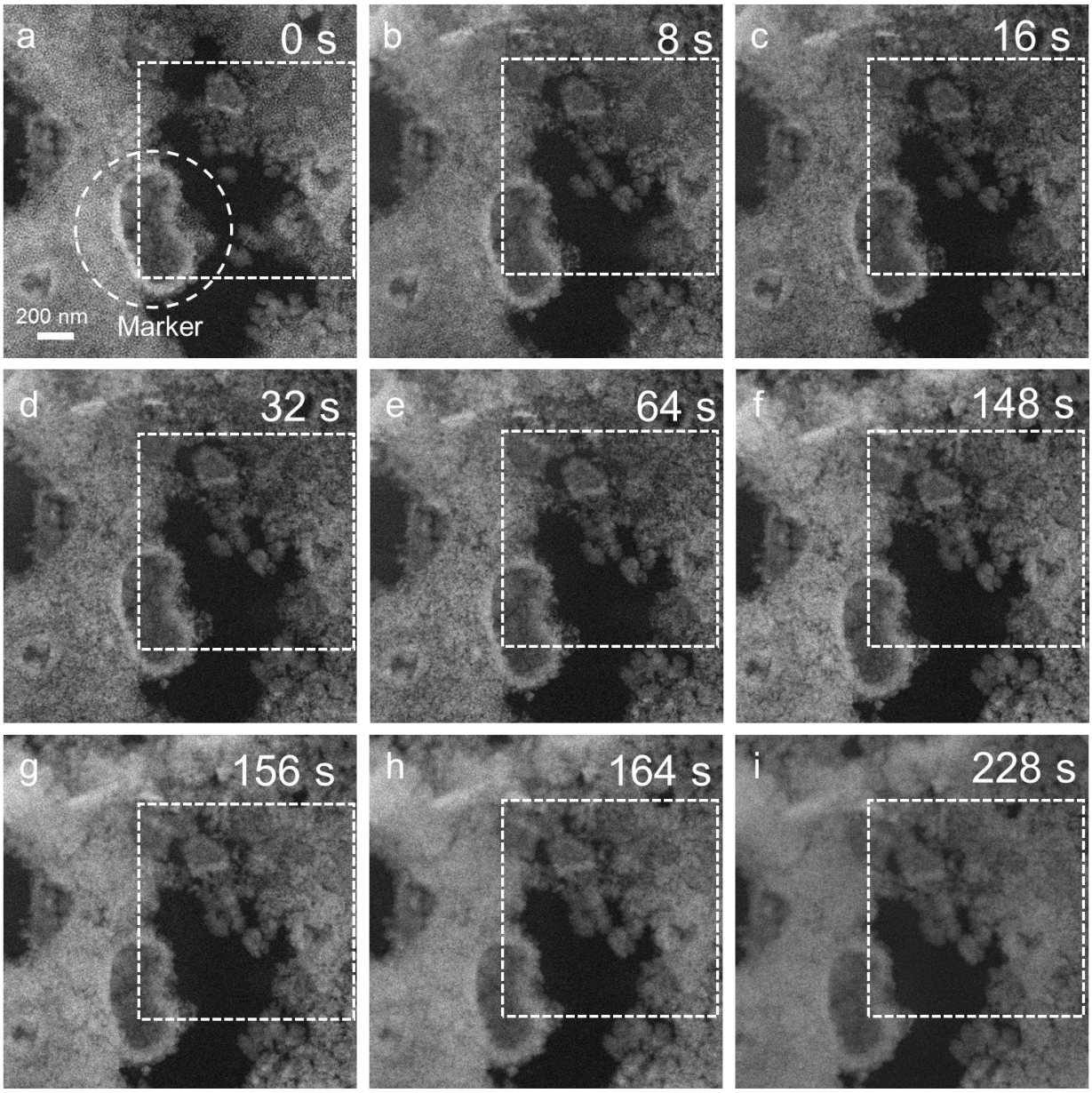

Supplementary Fig. 28. *Operando* EC-STEM images of 18 nm NPs at -0.8 V vs. RHE in CO_2-sat. 0.1 M $KHCO_3$ over an extended time period of about 4 min. The regions in the dashed boxes highlight structural changes shown in Figs 3i-k. The slight shifts of box positions are due to the sample drift in liquid over a long reaction time. Dynamic changes can be found in Supplementary Video 6. STEM videos were tracked at the region of interest by following the feature in the dashed circle serving as a "marker".

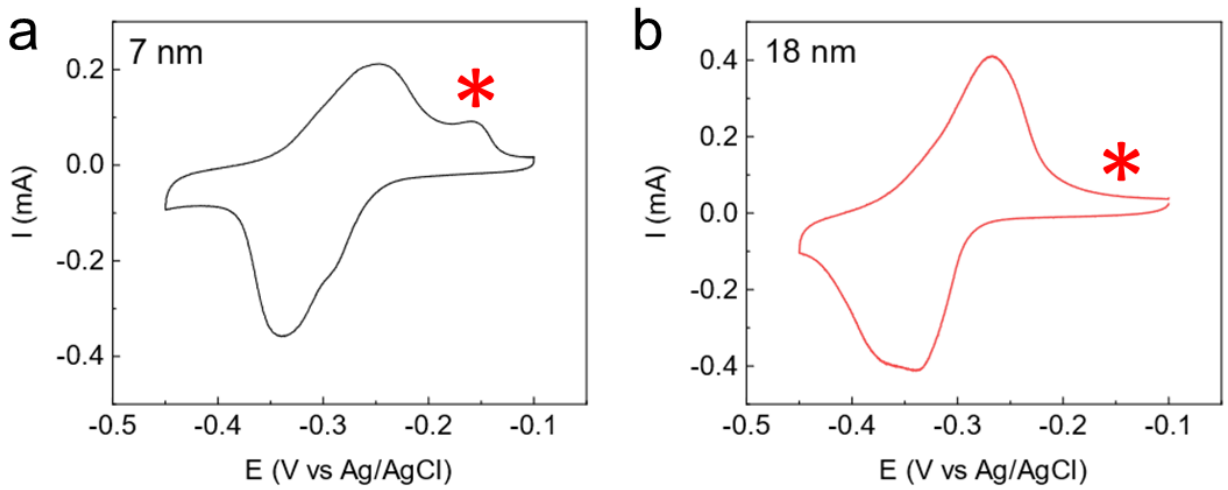

Supplementary Fig. 29. Cyclic voltammetry in the Pb underpotential deposition (UPD) potential range at 10 mV/s for (a) the 7 nm and (b) 18 nm Cu NP ensemble immediately after CO_2 electroreduction at -0.80 V vs. RHE. The voltammogram of the 7 nm Cu NP ensemble displays an anodic feature at -0.16 V vs. Ag/AgCl that is absent in the 18 nm Cu NP ensemble, which was correlated to undercoordinated and defective Cu sites,[43] as indicated by the red asterisks. This suggests that, unlike the 7 nm Cu NP ensemble, the 18 nm Cu NP ensemble does not form a large density of undercoordinated sites during the CO_2RR. Pb UPD was conducted in a solution of 0.1 M $NaClO_4$, 10 mM $HClO_4$, and 3 mM $Pb(II)(ClO_4)_2$. Six consecutive cycles were found to be consistent with each other and the fifth scan is reported.

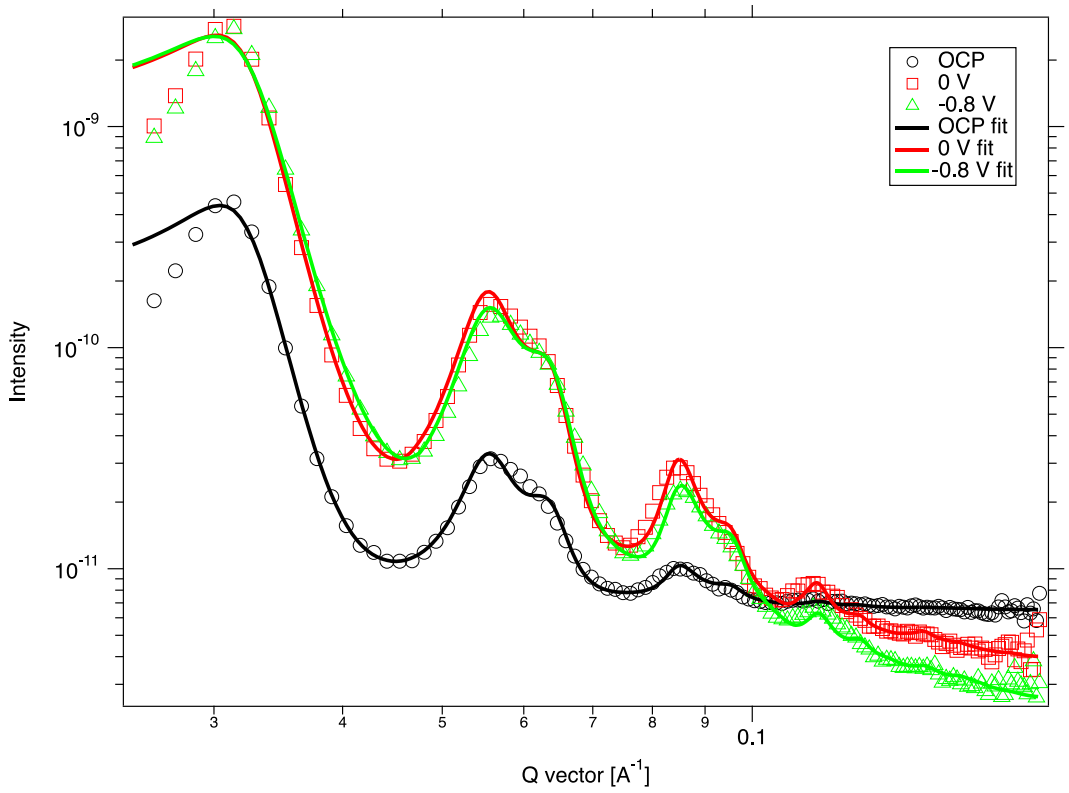

Supplementary Fig. 30. *Operando* resonance soft X-ray scattering data and corresponding fitting acquired at 934.4 eV. Good fitting result was achieved with a model of 2D hexagonal packed spherical particles with an inhomogeneous surface layer outside of the particle bulk. This is a good indication that there is a surface metallic Cu layer (Cu^S) that can be differentiated from the bulk Cu. The particle radius size was found to be 9.84 nm at 0 V and 9.55 nm for the -0.8 V respectively, suggesting that the average nanograin size at -0.8 V vs. RHE is smaller than that at 0 V vs. RHE by 2.9 Å with a relative fitting error of 0.2 Å. The surface layer thicknesses were ~0.5 nm for both 0 V and -0.8 V but the density of the surface layer of -0.8 V increased by ~20%, suggesting a denser packing at more negative potentials. Technical details of *operando* soft X-ray scattering studies were introduced in our recent work[34].

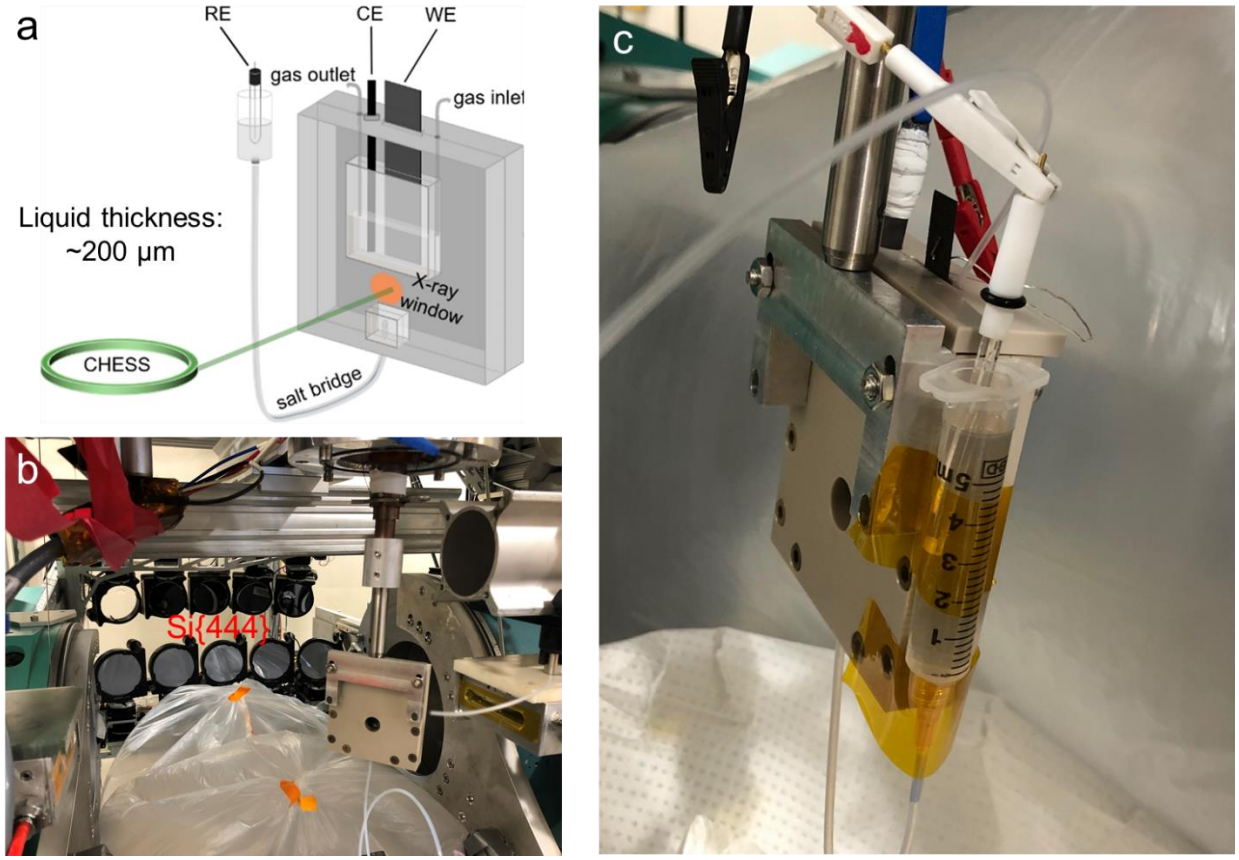

Supplementary Fig. 31. *Operando* HERFD XAS setup. (a) Schematic of the XAS electrochemical cell with a working electrode (WE, Cu NPs supported on carbon paper) and a counter electrode (CE, carbon rod) immersed in CO_2-sat. 0.1 M $KHCO_3$. The reference electrode (RE, Ag/AgCl in sat. KCl) was connected to the cell by a salt bridge to minimize the iR drops caused by the resistance in the thin liquid layer (< 200 μm) within the X-ray window. (b-c) Photos of the XAS cell operating at CHESS with five pairs of Si{444} single crystals to select Cu $K\alpha_1$ emission line for HERFD analysis with a high energy resolution on the order of ~1 eV.

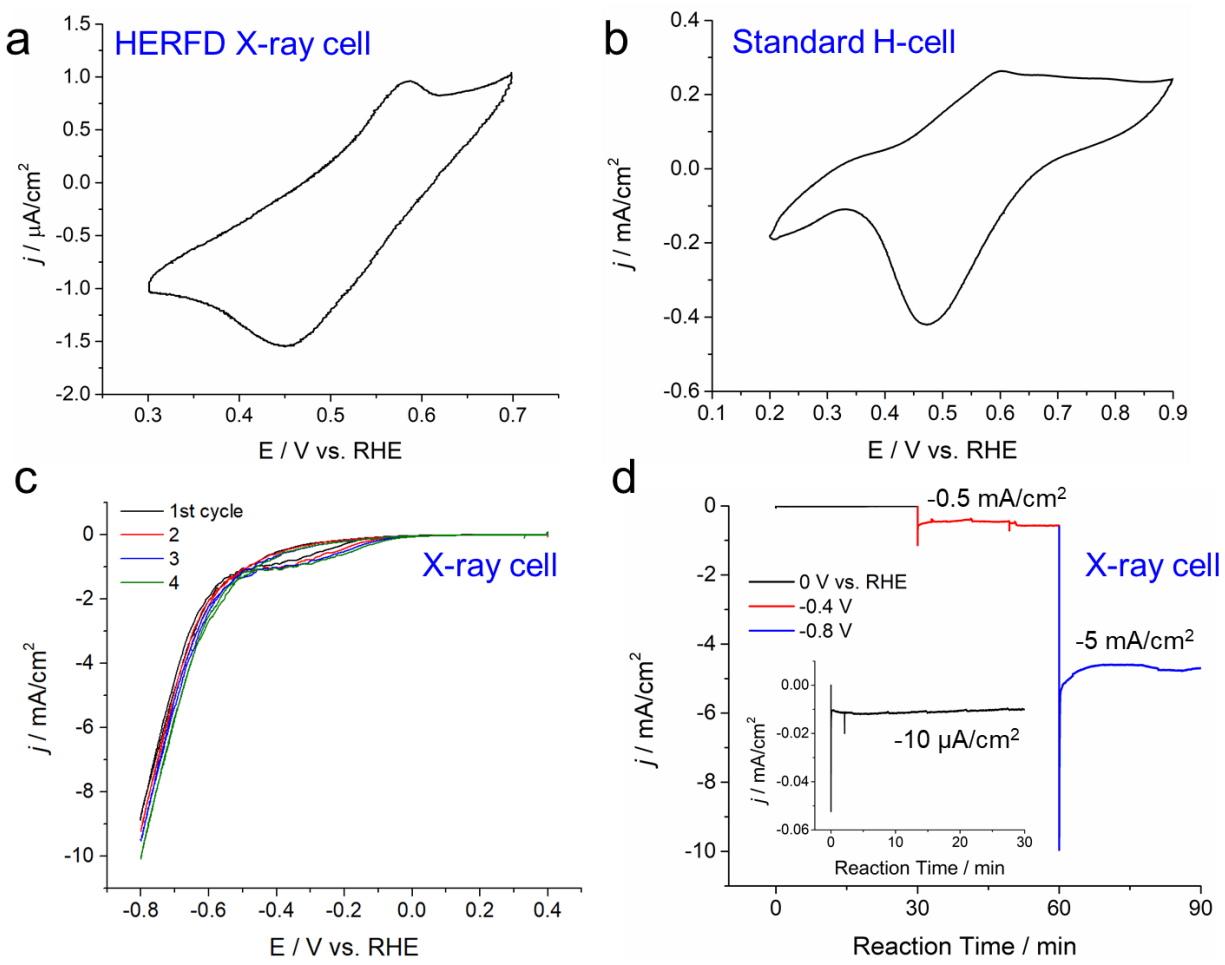

Supplementary Fig. 32. Electrochemical measurements in *operando* HERFD XAS cell. (a-b) CV profile of 7 nm NPs supported on carbon paper in CO_2-sat. 0.1 M $KHCO_3$ obtained from the XAS cell at 10 mV/s in (a), which shows a comparable reduction peak at ~0.45 V vs. RHE to the CV profile measured in a standard H-cell under the same test conditions at 50 mV/s in (b). (c) CV profiles of 7 nm NPs in the XAS cell shows good reproducibility among consecutive four cycles. (d) Chronoamperometry (CA) profiles of 7 nm NPs measured in the XAS cell at 0, -0.4, and -0.8 V vs. RHE.

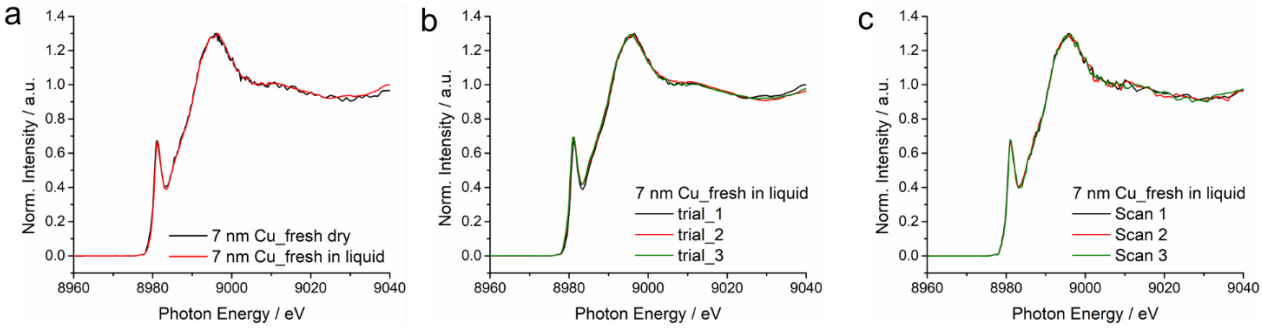

Supplementary Fig. 33. Negligible X-ray beam effects on the 7 nm Cu NP ensemble in electrolyte. HERFD XANES spectra of the Cu NP ensemble in dry form or immersed in CO_2-sat. 0.1 M $KHCO_3$ (a) and three independent trials (b) as well as three consecutive scans in electrolyte (c). All measurements showed no beam damage as reflected by the stability of the XANES spectra.

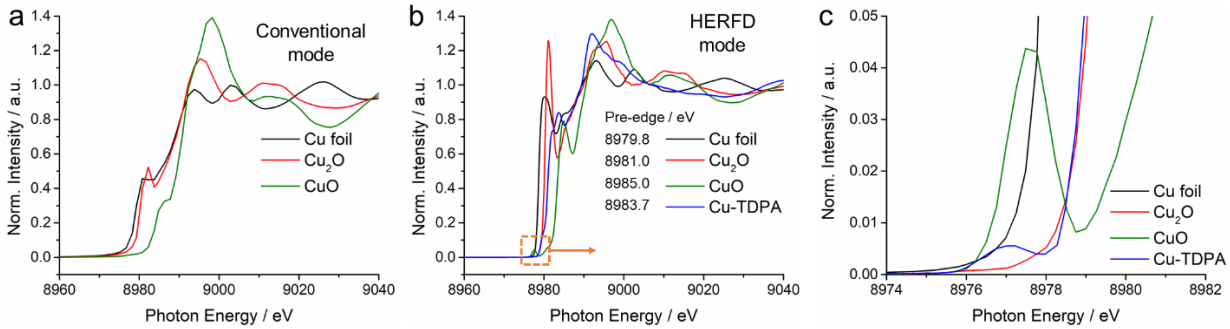

Supplementary Fig. 34. (a) XANES spectra of standard references of Cu foil, Cu_2O, and CuO were collected with a conventional solid-state fluorescence detector. (b) High-energy-resolution XANES spectra of the same reference samples, along with a Cu-TDPA compound, using the HERFD detector, showing much better resolved pre-edges at around 8980 eV. Inset lists the pre-edge energy of four reference samples. (c) Enlarged region from the dashed box in (b) clearly shows the pre-edge peak of CuO at 8977.6 eV due to the Jahn-Teller distortion, which was not resolvable in conventional XANES spectra in (a). In addition, Cu-TDPA shows a unique broad feature at 8977.0 eV benefiting from the remarkable sensitivity of HERFD XANES.

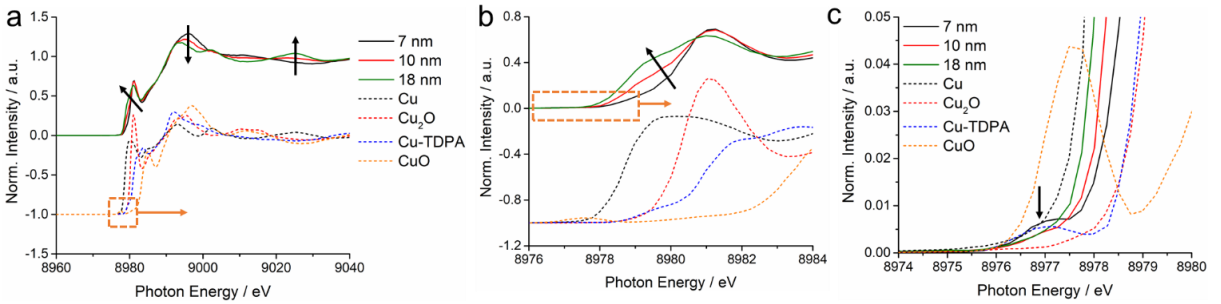

Supplementary Fig. 35. (a-b) Comparisons of as-synthesized 7, 10, and 18 nm Cu NP ensembles to four reference spectra. Enlarged dashed box in (a) is displayed in (b). Intensity of reference spectra has a y-offset to better show the progressive changes of XANES spectra of Cu NPs. A higher fraction of metallic Cu was observed as shown by the arrows as the particle size increased from 7 to 10 and 18 nm. (c) XANES spectra enlarged from the pre-edges in (b) exhibit that 7 nm NPs show a pre-edge peak at 8977.0 eV resembling that of Cu-TDPA, indicating the presence of TDPA ligand on 7 nm NPs. In comparison, this feature is less pronounced for 10 and 18 nm NPs which is possibly due to the higher volume ratio of bulk Cu signals of larger NPs, relative to surface Cu bound to TDPA.

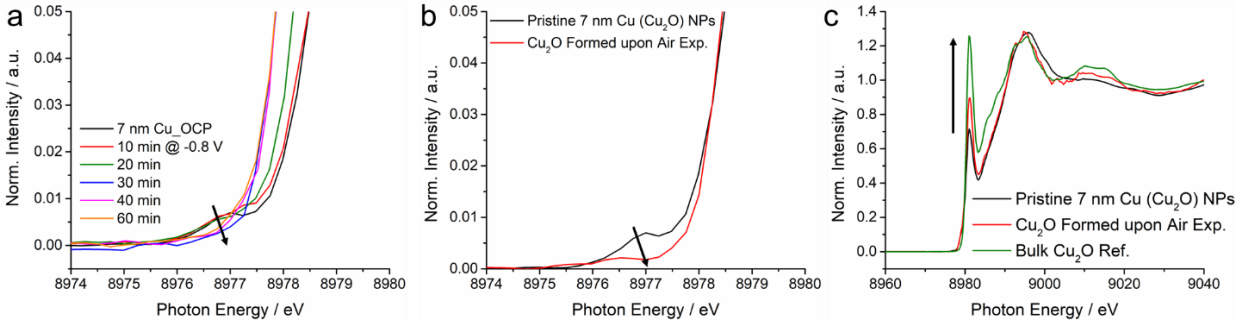

Supplementary Fig. 36. (a) HERFD XANES of 7 nm NPs showing the diminution of pre-edge peaks at 8977.0 eV at -0.8 V vs. RHE, indicating possible ligand desorption and less contributions from surface Cu as a result of growing particle sizes under bias. (b) The pre-edge peak remains absent in the Cu_2O formed after air exposure. The pre-edge peak feature at 8977 eV, assigned to Cu-TDPA bonding, rapidly disappeared under electroreduction, possibly due to the ligand desorption and concomitantly decreasing contributions of surface Cu of growing Cu nanograins. (c) HERFD XANES spectra of the 7 nm Cu NP ensemble, ~100 nm Cu_2O nanocubes, and μm-sized Cu_2O powder, showing a strong dependence of pre-edge intensity on particle sizes. The intermediate pre-edge intensity of Cu_2O nanocubes was ascribed to their particle sizes (~100 nm) in between pristine 7 nm oxidized NPs and μm-sized Cu_2O.

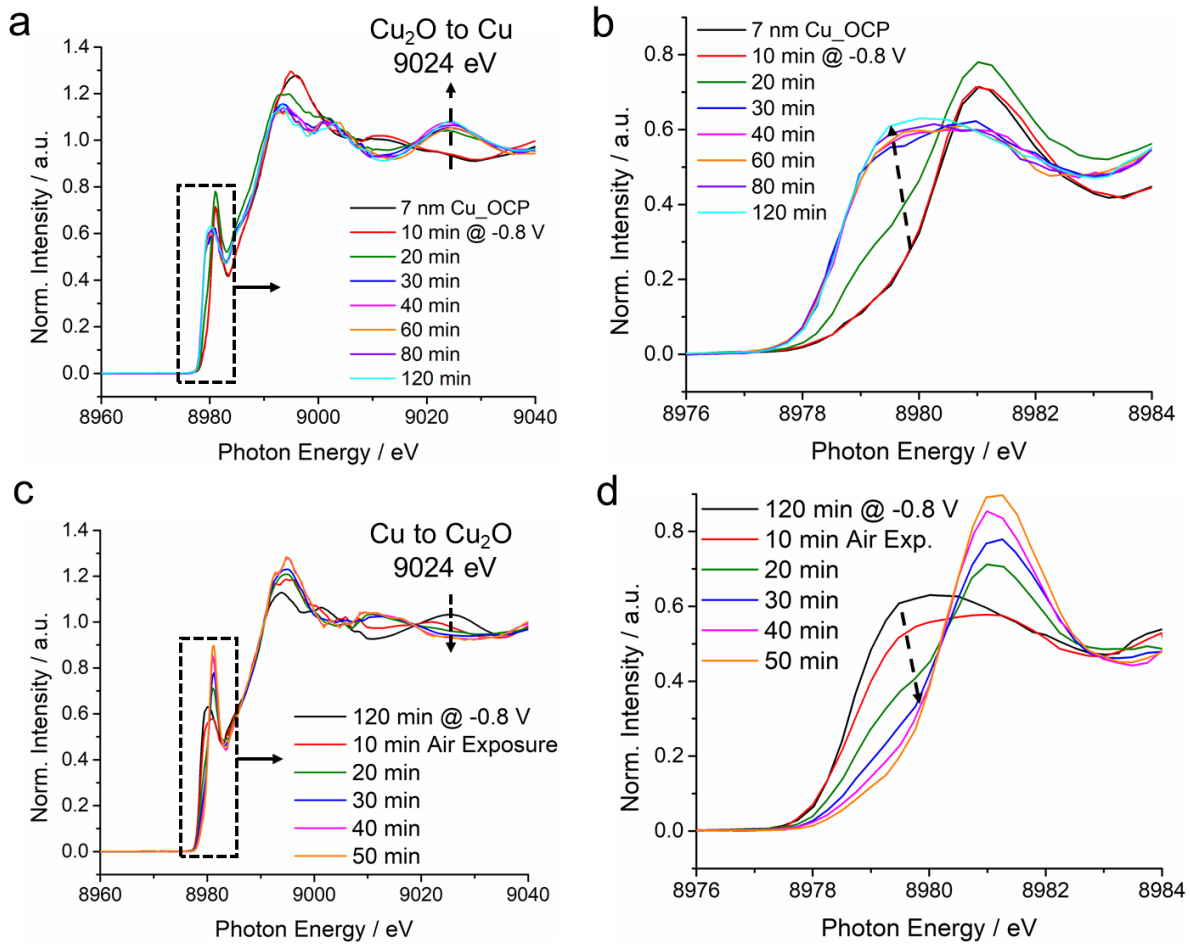

Supplementary Fig. 37. (a-b) XANES spectra of the 7 nm Cu NP ensemble at -0.8 V vs. RHE over the time period of 2 h. Both the (a) post-edge region at 9024 eV and the (b) enlarged pre-edge region show the progressive conversion from Cu_2O to metallic Cu nanograins, which was nearly complete after 30 min. (c-d) XANES spectra of the post-electrolysis 7 nm Cu NP ensemble upon air exposure for 50 min. At ~8979 eV in the pre-edge region and at 9024 eV in the post-edge region show the transition from metallic Cu to Cu_2O, which approached complete oxidation to Cu_2O after about 40 min.

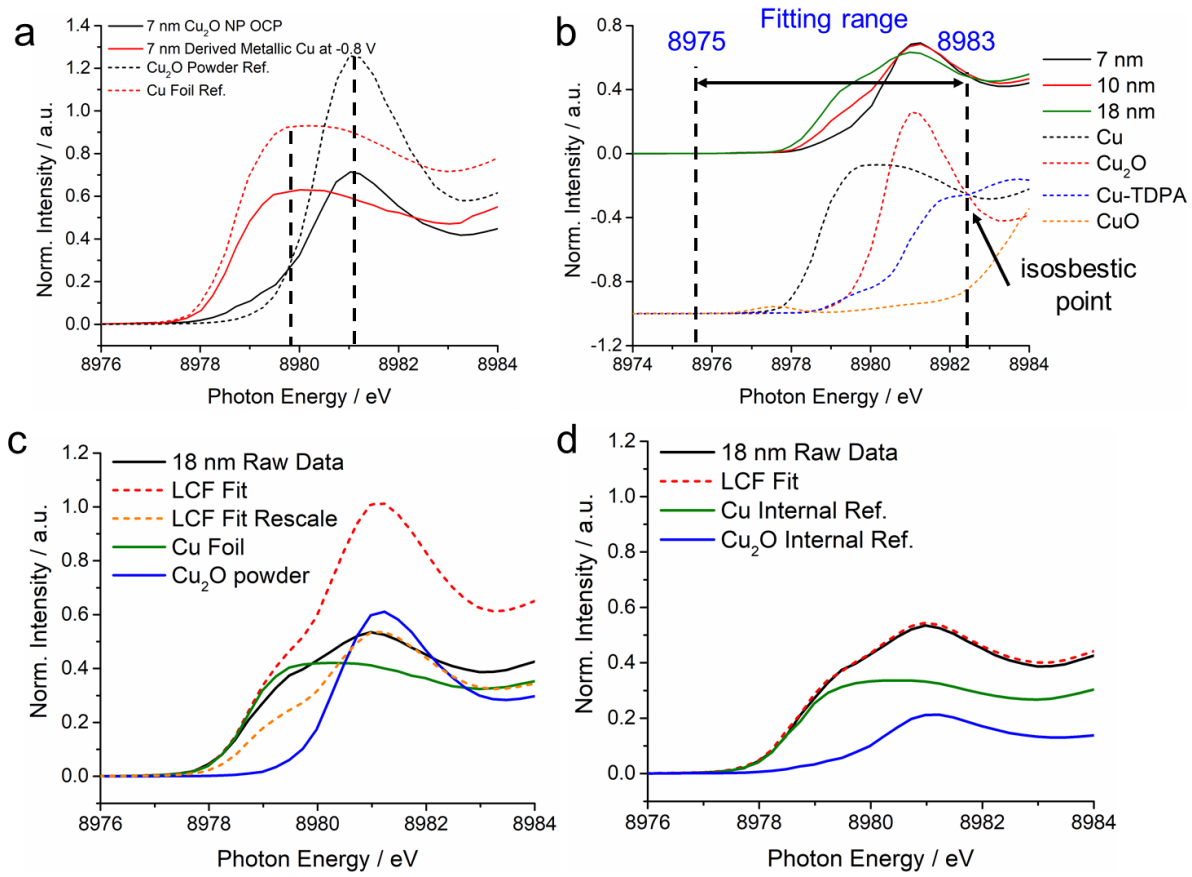

Supplementary Fig. 38. Methodology for quantitative analysis of HERFD XANES spectra. (a) Comparison of the 7 nm Cu NP ensemble and derived active metallic Cu structure to bulk Cu_2O and Cu references, showing the nearly same edge energies, indicating 7 nm NPs and derived metallic Cu can serve as the internal reference spectra. (b) The quantitative fitting range was selected from 8975 to 8983 eV at which all reference spectra share the same intensity, i.e. an isosbestic point. (c-d) The 18 nm Cu@Cu_2O NP ensemble was used as an example of mixed phases to assess which reference spectra would result in higher-quality linear combination fitting (LCF). The LCF fit using bulk Cu and Cu_2O references in (c) failed to capture the intensity and overall curvature of the pre-edge peak with a large relative error of 13% and a reduced χ^2 of 0.055. The LCF fit using the internal reference spectra resulted in a high-quality fitting of the entire pre-edge peak, giving 68% Cu and 32% Cu_2O with a small relative error of 1.1% and a reduced χ^2 of 0.000064. The criterion for a high-quality LCF fitting is a reduced χ^2 lower than 0.001.

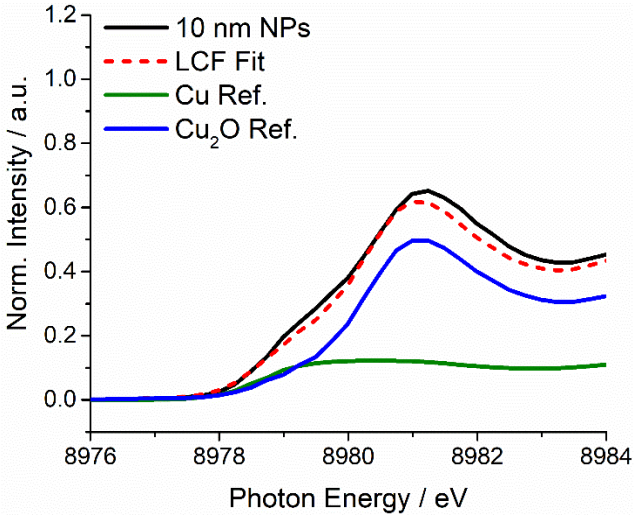

Supplementary Fig. 39. The LCF fit of HERFD XANES pre-edge of 10 nm NPs using the internal Cu and Cu_2O reference spectra, as performed for 18 nm NPs in Supplementary Fig. 38, resulted in 25% Cu and 75% Cu_2O with a relative error of 3.1% and a reduced χ^2 of 0.0053.

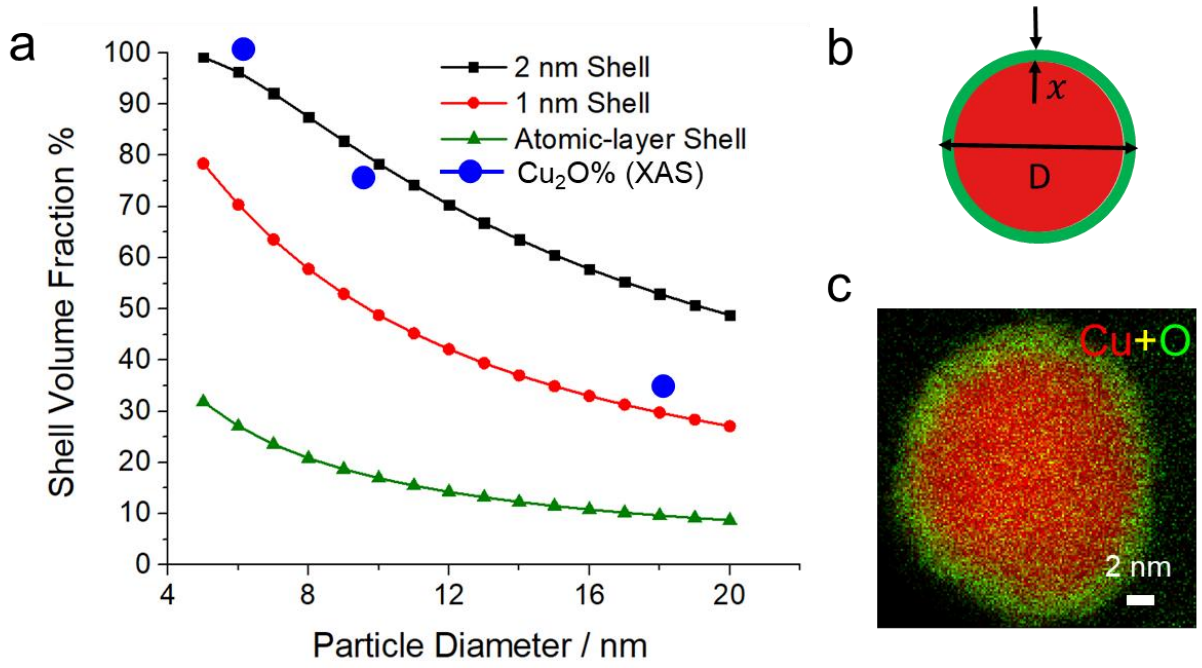

Supplementary Fig. 40. (a) Comparison of Cu_2O at.% estimated from the XAS fitting in Supplementary Figs. 38-39 with a simplified geometric calculation of oxide shell volume fraction assuming atomic-layer shell (2.5 Å for $Cu_2O\{111\}$), 1 and 2 nm shells as a function of particle sizes. (b) A geometric model of a spherical nanoparticle with a core diameter of D and oxide shell thickness of x. (c) An example of EELS composite map of 18 nm NPs with ~2 nm oxide shell.

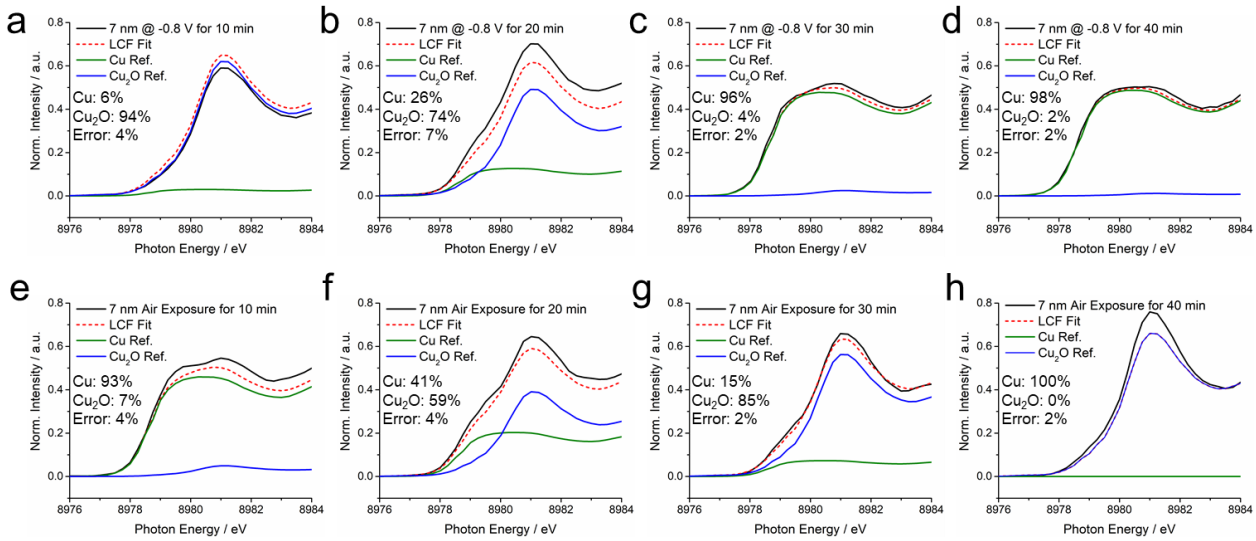

Supplementary Fig. 41. LCF fitting of the 7 nm Cu NP ensemble under CO_2RR conditions and upon post-electrolysis air exposure.

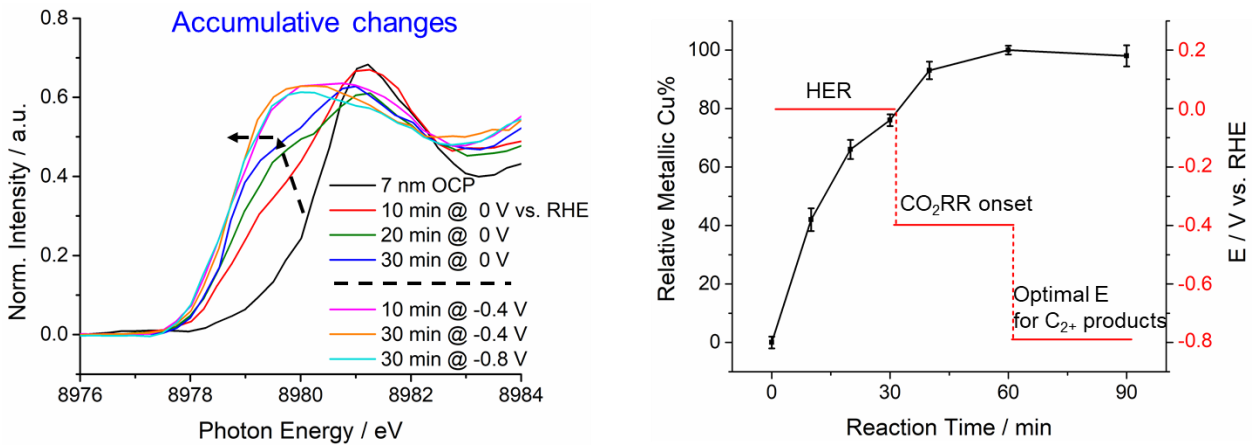

Supplementary Fig. 42. (a) HERFD XANES spectra of the 7 nm Cu NP ensemble at a series of potential steps and corresponding quantitative analysis of relative metallic Cu fraction. As applied potentials decreased from the OCP (~0.5 V vs. RHE) to 0 V, the HER occurred and about 75% Cu_2O was converted to metallic Cu. As potential decreased from 0 to the onset of the CO_2RR (about -0.4 V vs. RHE), all the remaining Cu_2O fully evolved into metallic Cu, which remained the metallic Cu structure as potentials decreased to -0.8 V.

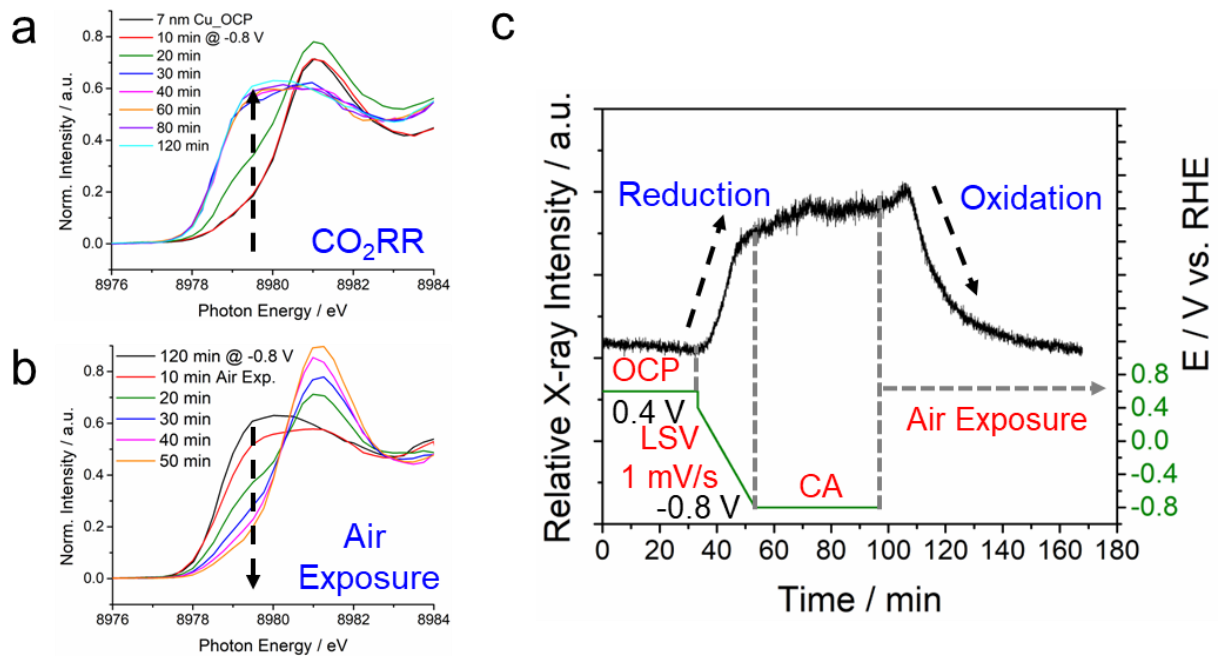

Supplementary Fig. 43. Dynamic tracking of valence state during the life cycle of 7 nm NPs at a constant photon energy of 8979.5 eV, as indicated by the black dashed arrows in (a-b). (c) The increase in X-ray intensity as the LSV from 0.4 to 0 V corresponds to the electroreduction of 7 nm NPs to fully metallic Cu nanograins. The "potential resolution" is 2 mV per X-ray event given a scan rate of 1 mV/s and 2 s per X-ray event. The X-ray intensity plateau at -0.8 V during CA process suggests that Cu remains metallic under reaction conditions and evolves post-electrolysis into Cu_2O cubes as shown in the X-ray intensity decay upon air exposure. We fixed the X-ray absorption energy at 8979.5 eV at which the relative signal intensity corresponding to valence changes achieves a maximum value. The dynamic tracking of valence states started at the OCP and showed a stable plateau over 30 min with no beam-induced damage. Then, a linear scan voltammetry (LSV) experiment was carried from 0.4 to -0.8 V vs. RHE at 1 mV/s, so that an electrode potential resolution of 2 mV was achieved with 2 seconds per X-ray acquisition event. Upon bias application, the signal intensity took off immediately which corresponds to the Cu_2O electroreduction to metallic Cu. The applied potential was then maintained at -0.8 V for 1 h which correlated with a metallic Cu as shown by the plateau of X-ray intensity with negligible fluctuations. Finally, upon stopping the reducing bias, the signal intensity started to steadily decay in agreement with the Cu reoxidation to Cu_2O. The slow reaction kinetics observed in the X-ray cell relative to the H-cell was ascribed to the thin-liquid configuration (~200 μm) which was designed to minimize background interruption associated with gas bubble formation during electrolysis.

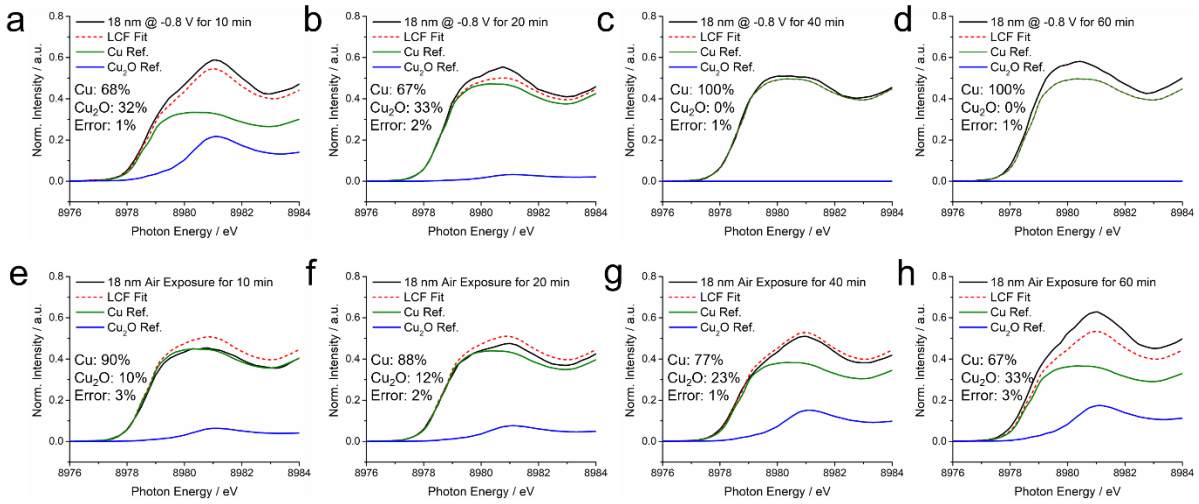

Supplementary Fig. 44. LCF fitting of the 18 nm Cu NP ensemble under CO_2RR conditions and upon post-electrolysis air exposure.

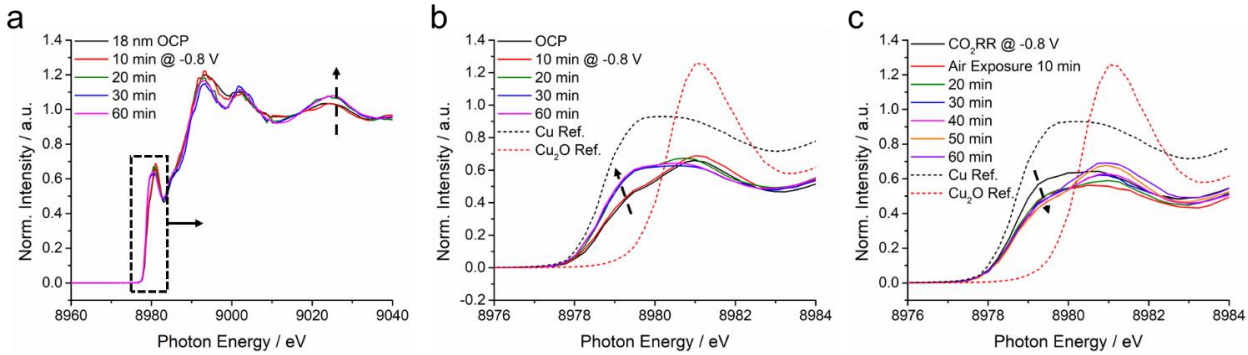

Supplementary Fig. 45. (a-b) *Operando* XANES spectra of the 18 nm Cu NP ensemble at -0.8 V vs. RHE over the time period of 2 h. Both (a) at 9024 eV in the post-edge region and (b) the pre-edge peaks show the complete reduction of the Cu@Cu_2O surface oxide to metallic Cu after 20 min. (c) XANES spectra of the post-electrolysis 18 nm Cu NP ensemble upon air exposure. The peak at ~8979 eV in the pre-edge region shows the progressive transition from metallic Cu to a mixed phase of Cu and Cu_2O.

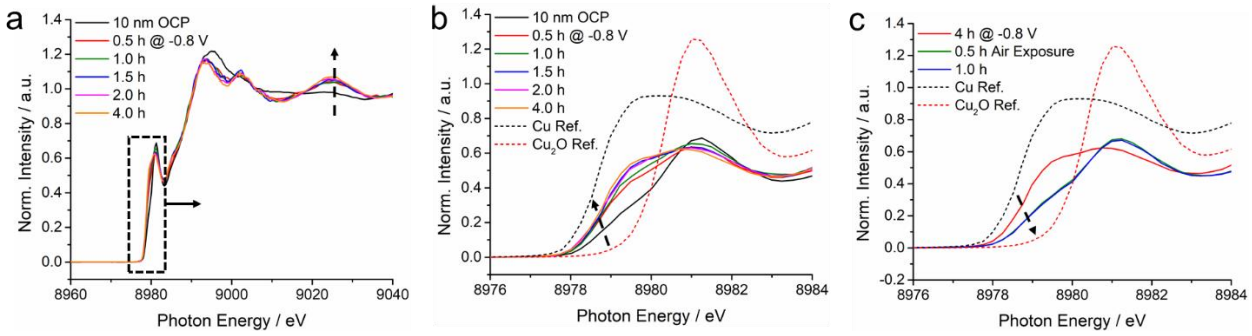

Supplementary Fig. 46. (a-b) XANES spectra of the 10 nm Cu NP ensemble at -0.8 V vs. RHE over the time period of 2 h. Both (a) at 9024 eV in the post-edge region and (b) the pre-edge peaks show the reduction of the Cu@Cu_2O surface oxide to metallic Cu. (c) XANES spectra of the post-electrolysis 10 nm Cu NP ensemble upon air exposure. The pre-edge peak at ~8979 eV shows the progressive transition from metallic Cu to a mixed phase of Cu and Cu_2O.

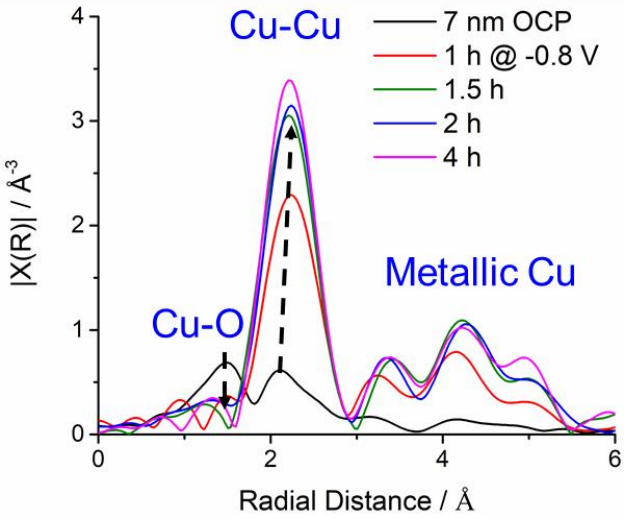

Supplementary Fig. 47. *Operando* time-resolved k^2-weighted Fourier transformed EXAFS of the 7 nm Cu NP ensemble during electroreduction at -0.8 V vs. RHE.

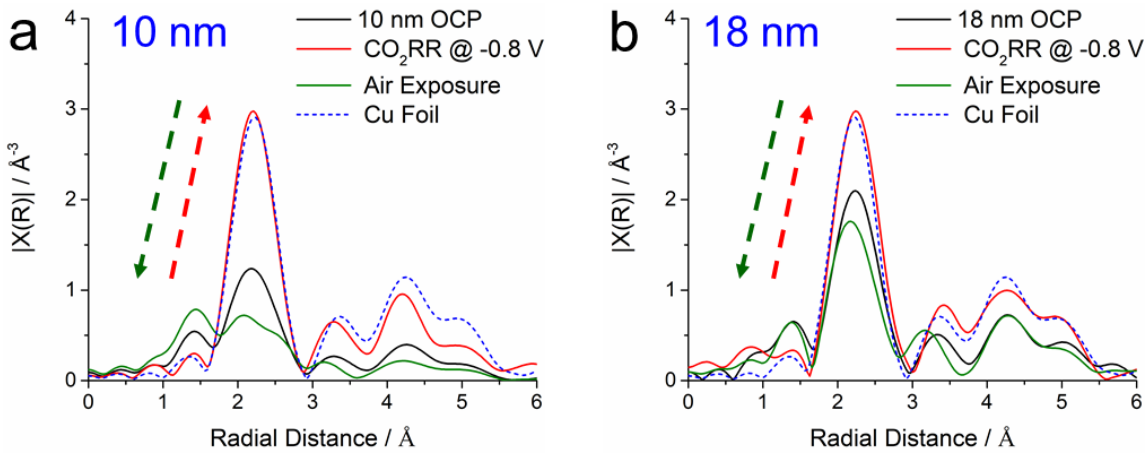

Supplementary Fig. 48. *Operando* EXAFS of 10 and 18 nm Cu NP ensembles before, during, and upon electrolysis air exposure and their comparison to metallic Cu foil.

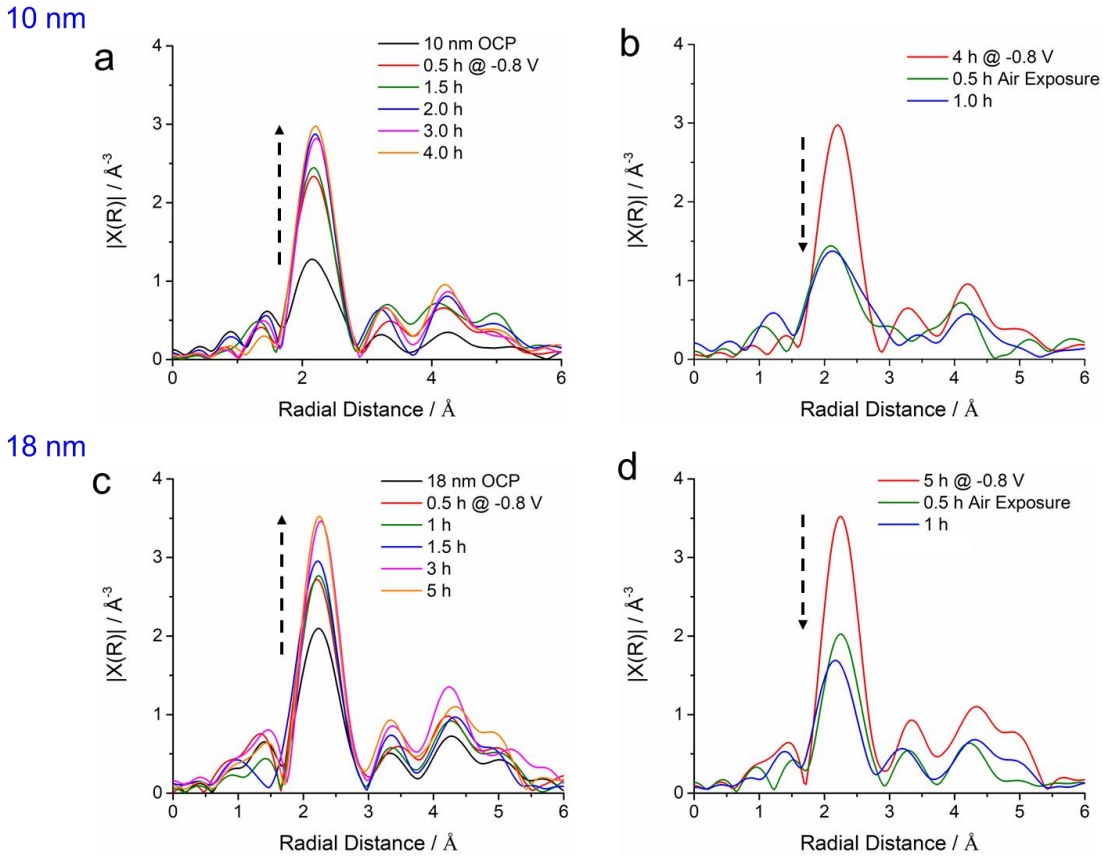

Supplementary Fig. 49. *Operando* time-resolved k^2-weighted Fourier transformed EXAFS of the 10 nm (a-b) and 18 nm (c-d) Cu NP ensembles during electrolysis and upon post-electrolysis air exposure.

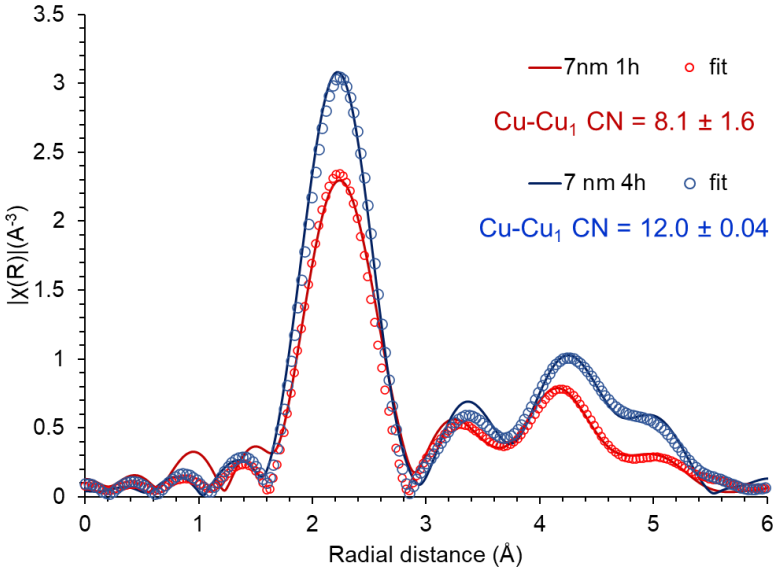

Supplementary Fig. 50. Fitting (circles) of the experimental EXAFS (line) of the 7 nm Cu NP ensemble at -0.8 V vs. RHE for 1 h (red) and 4 hrs (blue) under CO_2RR conditions. Cu-Cu_1 CN indicates the coordination number of the nearest Cu-Cu bond in a FCC Cu geometry. At the initial stage of particle aggregation (1 h electrolysis), an average CN of 8 suggests the presence of the undercoordinated Cu sites, which is consistent with the presence of stronger binding sites in Pb UPD measurements (Supplementary Fig. 29). After sufficiently long time, the structure of active Cu nanograins approaches a steady state with sizes of 50-100 nm, which leads to a surface Cu monolayer contributing to less than 5% of the total volume of Cu nanograins.

NP sizes	Active Cu Nanograins %	C_{2+} FE% at -0.8 V vs. RHE
7 nm NPs	100 ± 2	44.3 ± 8
10 nm NPs	75 ± 3	27.2 ± 4
18 nm NPs	32 ± 2	6.9 ± 2

Supplementary Table 1. Structure-activity correlation of the 7, 10, and 18 nm Cu NP ensembles as plotted in Fig. 4f. Quantification of the fraction of active Cu nanograins based on HERFD XANES spectra with error bars from linear combination fitting. Quantification of C_{2+} faradaic efficiency as plotted in Fig. 4g with error bars was calculated from three independent measurements.

		7 nm		10 nm		18 nm	
	H_2	34.68	±3.54	46.97	±0.31	47.35	±2.94
C_1	CO	10.95	±1.57	13.73	±4.14	21.82	±4.21
	CH_4	0.27	±0.20	0.10	±0.05	0.10	±0.01
	Formate	9.75	±2.82	11.95	±2.03	23.83	±2.48
	MeOH	0.03	±0.02	0.02	±0.03	0.02	±0.03
C_2	C_2H_4	25.79	±6.37	14.09	±2.25	1.79	±0.54
	C_2H_6	0.35	±0.22	0.46	±0.16	0.16	±0.05
	EtOH	9.69	±1.74	5.83	±1.77	1.99	±0.46
	Glycolaldehyde	0.21	±0.09	0.17	±0.15	0.00	±0.00
	Acetate	1.06	±0.12	1.03	±0.05	0.64	±0.05
	Acetaldehyde	0.45	±0.05	0.16	±0.15	0.09	±0.15
C_3	Propanol	5.52	±0.33	4.96	±0.70	1.95	±0.68
	Allyl OH	0.96	±0.24	0.47	±0.41	0.19	±0.18
	Acetone	0.15	±0.01	0.05	±0.05	0.05	±0.09
	Propionaldehyde	0.15	±0.05	0.00	±0.00	0.00	±0.00

Supplementary Table 2. Faradaic efficiency (%) of CO_2 reduction products of the 7, 10, and 18 nm Cu NP ensemble at -0.8 V vs RHE. Standard deviation corresponds to three independent measurements.

E / V vs. RHE	I / mA	H_2%	CO%	CH_4%	$HCOO^-$%	C_2H_4%	EtOH%	PrOH%	J_{C2+} / (A/gCu)
-0.85	200	13.3	25.6	0	5.5	39	13.1	4.7	1136
-0.88	300	12.0	26.0	0	4.4	40	13.2	4.6	1734

Supplementary Table 3. Faradaic efficiency (%) of CO_2 reduction products of the 7 nm Cu NP ensemble in a flow-cell gas diffusion electrode (GDE) configuration at a Cu mass loading of 100 μg/cm^2 on a carbon paper working electrode. Additional scale-up of the GDE device with a larger-area electrode and higher Cu loading can help assess the practical applications of Cu ensemble catalysts and is under current investigation.

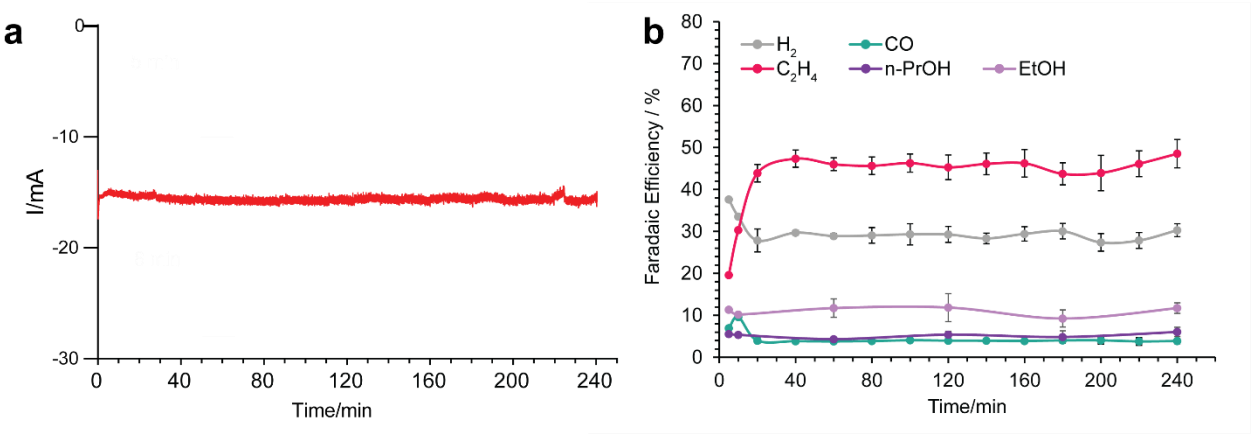

Supplementary Fig. 51. CO_2RR performance of the 7 nm Cu NP ensemble in an H-cell in terms of activity (a) and selectivity (b) over 4 hours of electrolysis at -0.8 V vs. RHE.

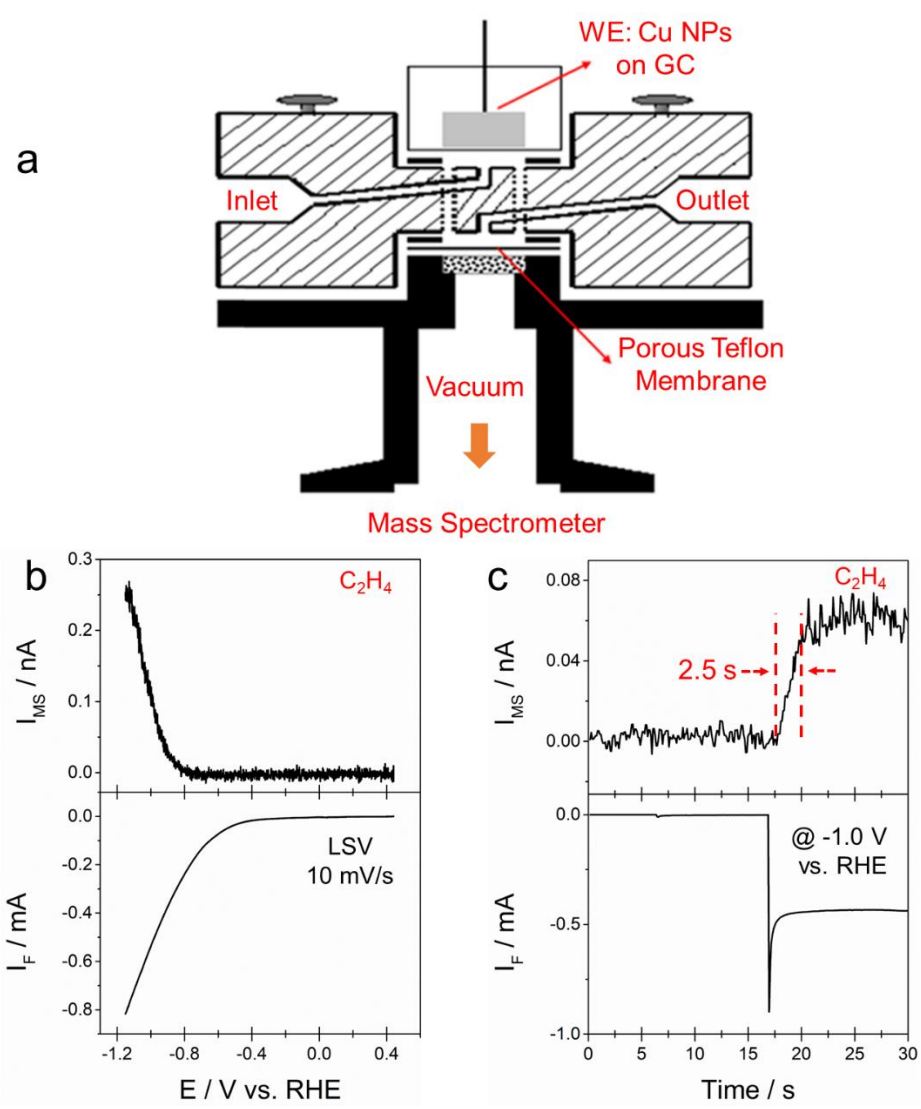

Supplementary Fig. 52. (a) *Operando* DEMS setup with dual thin-layer flow cell and (b-c) measurements of 7 nm Cu NP ensembles on glassy carbon (GC) electrodes. The customized dual thin-layer flow DEMS cell enables second-level rapid detection of gas products during CO_2RR. The flowing electrolyte (CO_2-sat. 0.1 M $KHCO_3$) interfaces with a porous Teflon membrane that allows the transport of gaseous products into the vacuum chamber while preventing electrolyte leakage. (b) DEMS measurements of the 7 nm Cu NP ensemble in an LSV scan show a steady increase of C_2H_4 yield in terms of MS current (m/z = 26 for the fragment of $C_2H_2^+$). (c) A potential step to -1.0 V vs. RHE shows the formation of C_2H_4 can reach a steady state in 2.5 s, demonstrating the significantly higher temporal resolution of *operando* DEMS setup. It should be noted that the response time of 2.5 s originates from the slow flow rate of 10 μL/s and only represent a lower limit of the actual fast reaction kinetics of C_2H_4 production. Technical details of DEMS can be found in our previous work[39].

Supplementary Note for structure and activity of 5 nm NP ensemble.

In order to provide a proof of the concept in the proposed strategies on smaller Cu clusters, we have successfully synthesized a smaller NP ensemble (5 nm) with the same TDPA ligand by optimizing synthetic conditions, so that the structure and activity comparisons between 5 nm NP and 7-18 nm NP ensemble are rigorous with the same surface chemical environment before CO_2RR.

As shown in Supplementary Fig. 53, HAADF-STEM images suggest a monodisperse particle size distribution (PSD) of 5.1 ± 0.4 nm and atomic-scale lattice images show that 5 nm NPs are polycrystalline Cu_2O NPs. Given the even smaller size of the 5 nm Cu NP ensemble, relative to the 7 nm Cu NP ensemble, pristine 5 nm Cu NPs are more reactive and fully oxidized to Cu_2O NPs when exposed to air right after colloidal synthesis.

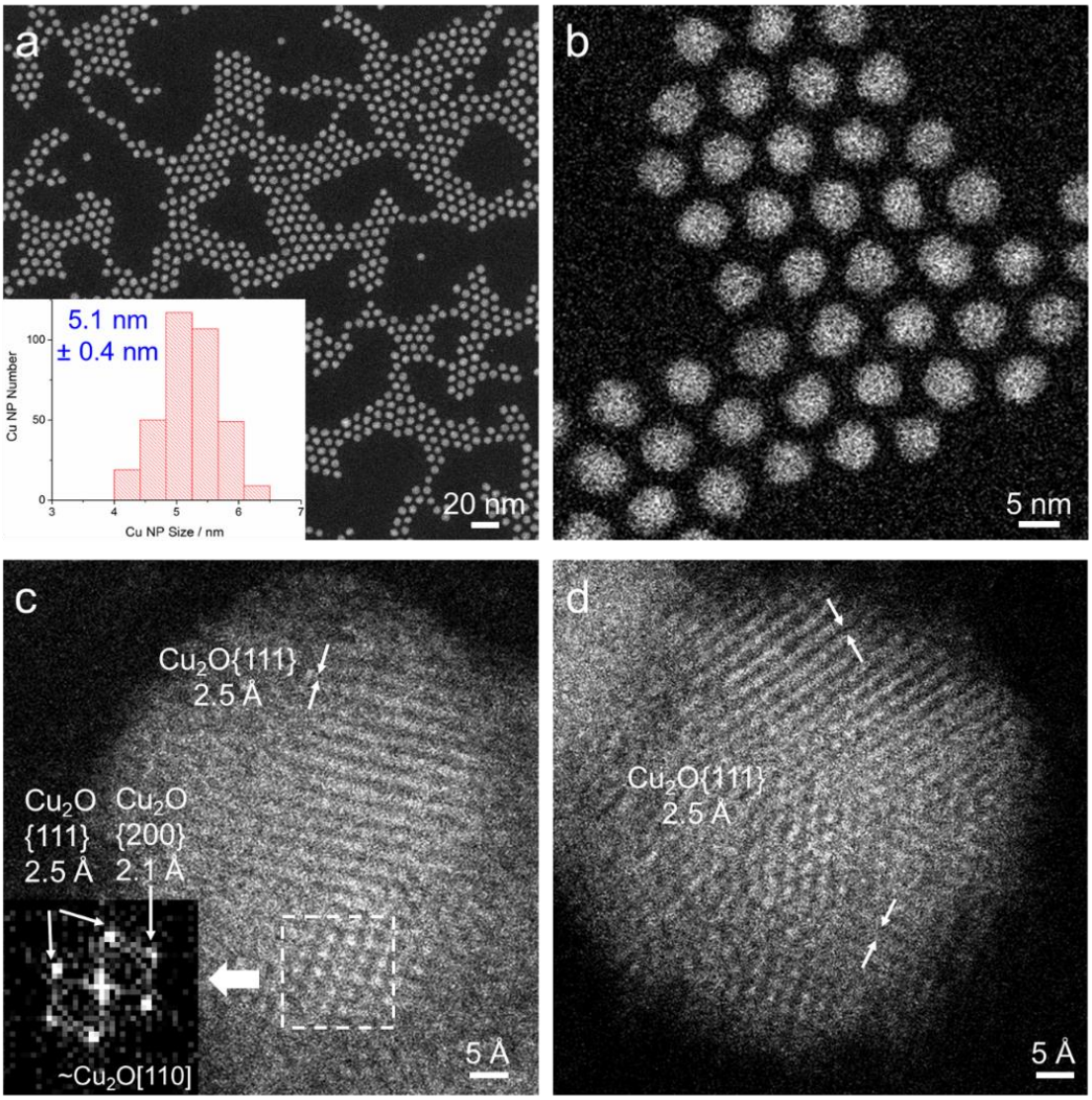

Supplementary Fig. 53. (a-b) HAADF-STEM images of the 5 nm Cu NP ensemble. Inset: particle size distribution of 5.1 ± 0.4 nm (one S_d). (c-d) Atomic-scale STEM images of individual 5 nm Cu NPs.

The 5 nm Cu NP ensemble showed a distinctly higher C_{2+} selectivity (55%) at a lower Cu mass loading of 49 μg/cm^2, relative to that of the 7 nm Cu NP ensemble (44% C_{2+} at a Cu loading of 69 μg/cm^2) (Supplementary Fig. 54 and Table 4). The Cu loading of the 5 nm Cu NP ensemble was controlled to be $\frac{5}{7}$ of the 7 nm Cu NP ensemble, in order to achieve a comparable electrochemical surface area (ECSA), since the projected surface area of one spherical NP is inversely proportional to the NP size.

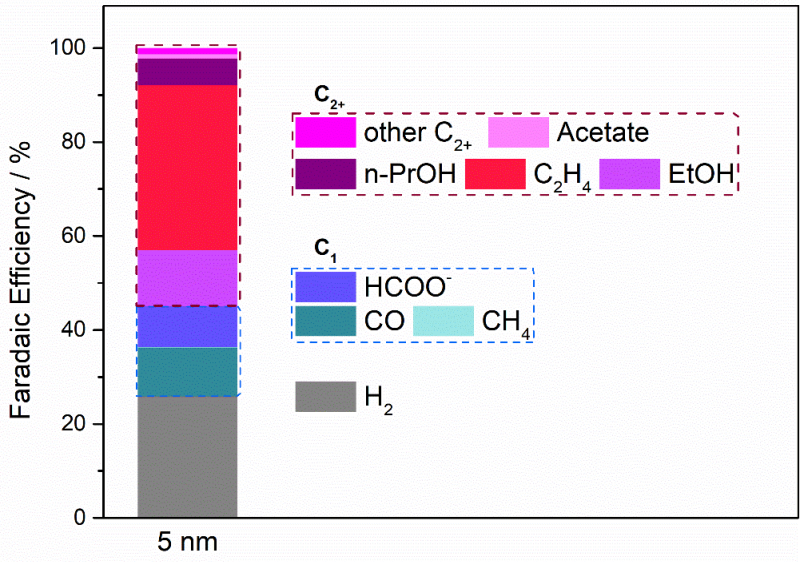

Supplementary Fig. 54. (a) CO_2RR performance of the 5 nm Cu NP ensemble measured at -0.8 V vs. RHE in 0.1 M $KHCO_3$ at a CO_2 flow rate of 20 mL/min in H-cell.

		5 nm		**7 nm**	
	H_2	25.92	±3.44	34.68	±3.54
C_1	CO	10.36	±2.22	10.95	±1.57
	CH_4	0.14	±0.12	0.27	±0.20
	Formate	8.62	±2.52	9.75	±2.82
	MeOH	0.0	±0.0	0.03	±0.02
C_2	**C_2H_4**	**35.17**	**±3.45**	**25.79**	**±6.37**
	C_2H_6	0.0	±0.0	0.35	±0.22
	EtOH	11.96	±2.42	9.69	±1.74
	Glycolaldehyde	0.0	±0.0	0.21	±0.09
	Acetate	0.91	±0.16	1.06	±0.12
	Acetaldehyde	0.24	±0.05	0.45	±0.05
C_3	Propanol	5.68	±0.14	5.52	±0.33
	Allyl OH	0.59	±0.08	0.96	±0.24
	Acetone	0.09	±0.02	0.15	±0.01
	Propionaldehyde	0.35	±0.06	0.15	±0.05
Average Total C_{2+}		**55.0**	±4	**44.3**	±8

Supplementary Table 4. Faradaic efficiency (%) of CO_2 reduction products of 5 and 7 nm Cu NP ensemble. Standard deviation corresponds to three independent measurements.

We then employed *operando* EC-STEM to directly visualize the structural evolution of the 5 nm Cu NP ensemble under CO_2RR conditions (Supplementary Fig. 55 and Video 7). A linear sweep voltammetry (LSV) scan from 0.4 to 0 V vs. RHE was used to trigger H_2 bubble formation so that the initial formation of Cu nanograins could be captured (Supplementary Fig. 55a). A beam-dose control experiment before applying potentials was performed for 40 s to ensure no beam damage (Supplementary Video 7). At -0.8 V vs. RHE, Cu nanograins continued to grow and approached a steady-state morphology (50-100 nm) after 60 s (Supplementary Fig. 55a-f). To better resolve the 5 nm Cu NP-derived Cu nanograins, higher-quality *operando* STEM images were acquired for a 10-time longer acquisition time in a thinner liquid-layer region (Supplementary Fig. 56a-b). 5 nm NP ensemble evolved into similar Cu nanograins with irregular (likely polycrystalline) morphology, when compared to 7 nm Cu NP-derived Cu nanograins (Supplementary Fig. 56c).

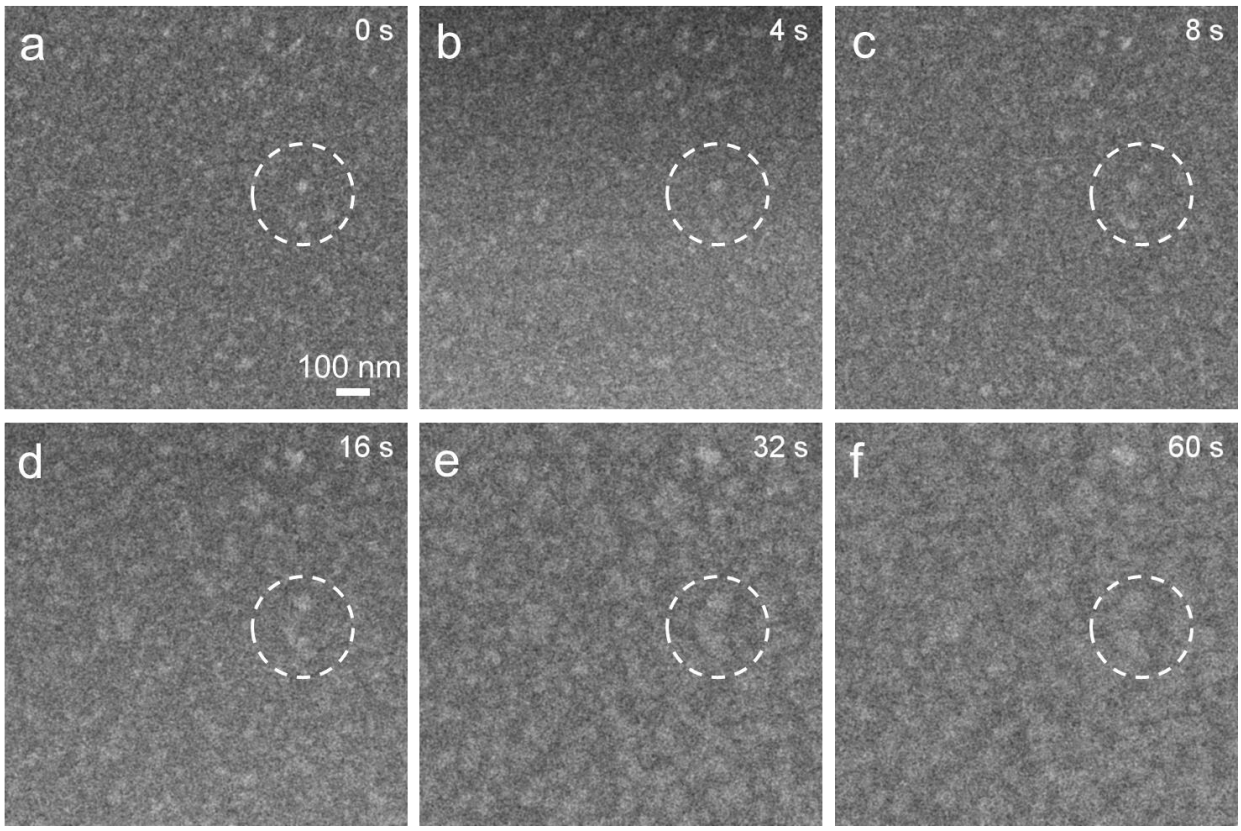

Supplementary Fig. 55. *Operando* EC-STEM videos of 5 nm Cu NP ensemble at -0.8 V vs. RHE in CO_2-saturated 0.1 M $KHCO_3$. Dashed circles highlight the growth of several Cu nanograins from initial sizes of sub-20 nm to steady-state sizes of ~100 nm. The corresponding *operando* STEM videos can be found in Supplementary Video 7.

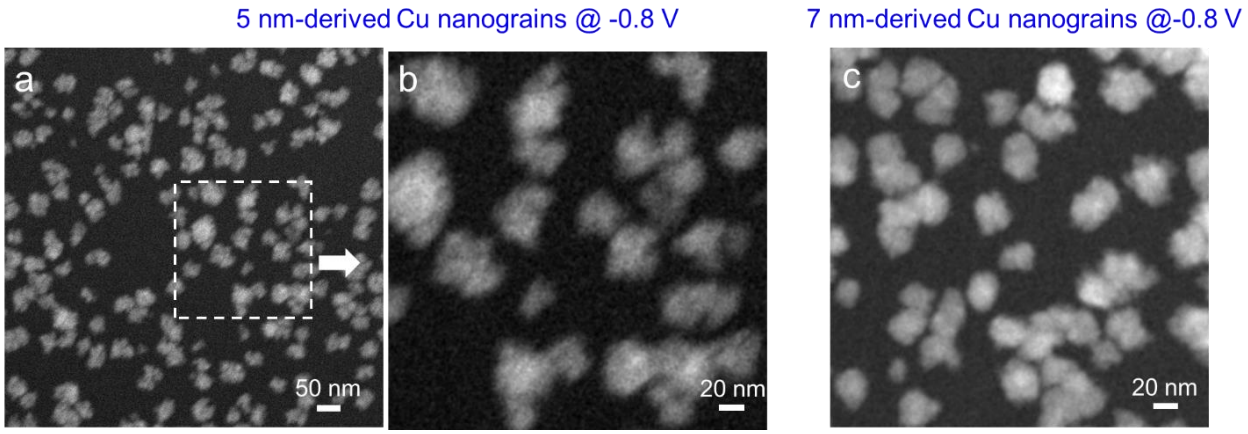

Supplementary Fig. 56 (a-b) *Operando* STEM images of 5 nm Cu NP-derived Cu nanograins after STEM videos at -0.8 V vs. RHE acquired for 40 s. (c) For comparison, *operando* steady STEM images of 7 nm Cu NP-derived Cu nanograins after STEM videos at -0.8 V vs. RHE adapted from main Fig. 2g.

Finally, SEM images of the 5 nm Cu NP ensemble on carbon paper before and after CO_2RR measurements in H-cell show that 5 nm Cu NP-derived Cu nanograins evolved into a similar final state of Cu_2O nanocubes upon post-electrolysis air exposure (Supplementary Fig. 57), when compared to that of 7 nm Cu NP ensemble (Fig. 2k). This is well consistent with the electroreduction/reoxidation cycle of 7-18 nm Cu NP ensembles as shown in main Fig. 1.

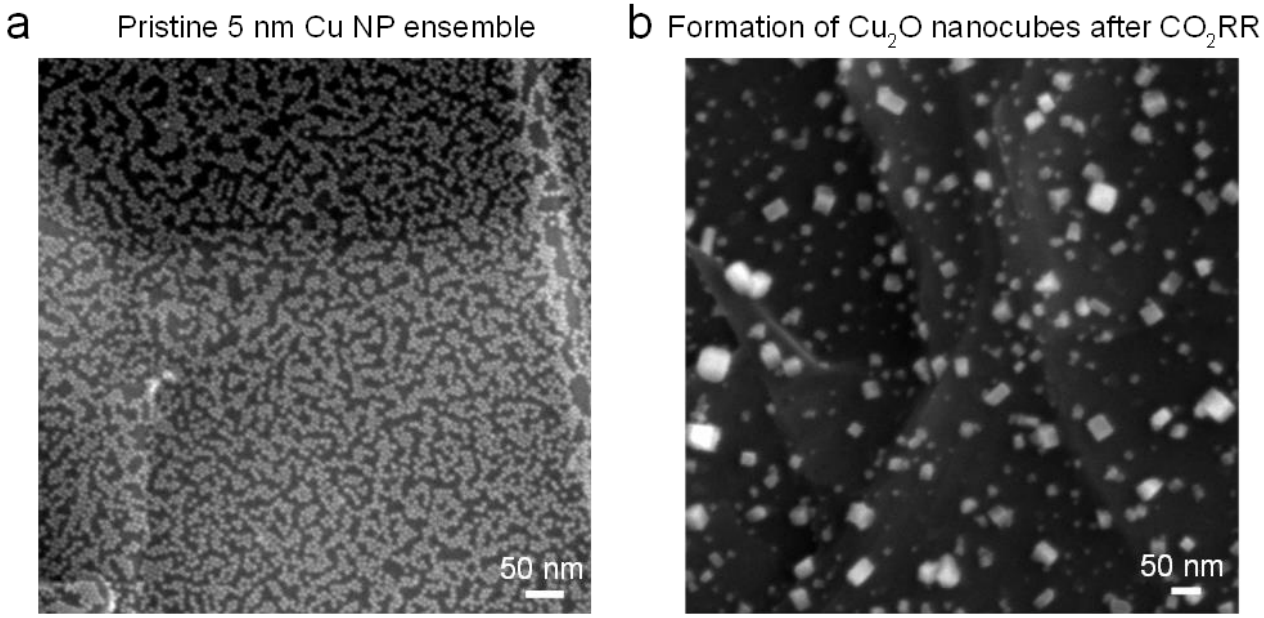

Supplementary Fig. 57. SEM images of pristine 5 nm Cu NP ensemble on carbon paper and the subsequent formation of Cu_2O nanocubes post-electrolysis in the H-cell and after air exposure.

In summary, we have validated that the strategy of further decreasing particle size while maintaining a similar evolution behavior of the Cu NP ensemble indeed contributes to an enhanced C_{2+} selectivity at a lower Cu loading. This indicates that a smaller Cu NP ensemble have a better

atomic efficiency for converting Cu NPs into active Cu sites for C-C coupling. *Operando* EC-STEM images and post-electrolysis SEM images provide strong evidence that the 5 nm Cu NP ensemble evolves into similar Cu nanograins during CO_2RR followed by similar subsequent post-electrolysis oxidation to Cu_2O nanocubes upon air exposure, relative to the 7 nm Cu NP ensemble. This indicates that the higher C_{2+} selectivity of the 5 nm Cu NP ensemble is likely due to the formation of a higher density of Cu nanograin boundaries, relative to the 7 nm Cu NP ensemble.

Supplementary Video Captions

Supplementary Video 1. *Operando* EC-STEM videos of Cu NPs under CV scan in CO_2-sat. 0.1 M $KHCO_3$. A H_2 bubble is triggered at 8 s (~0 V vs. RHE) to create a thin liquid film and significantly enhanced spatial resolution.

Supplementary Video 2. *Operando* EC-STEM videos of 7 nm NP ensemble at 0 V vs. RHE for 28 s. Note that STEM videos were acquired without potential applied from -16 to 0 s in order to show no beam-induced damage at a dose rate of ~12.5 e^-/nm^2s (dose of ~50 e^-/nm^2 per frame).

Supplementary Video 3. *Operando* EC-STEM videos of 7 nm NP ensemble at -0.8 V vs. RHE for 88 s.

Supplementary Video 4. *Operando* EC-STEM videos of Cu_2O nanocubes, formed from 7 nm NP-derived Cu nanograins upon air exposure at -0.8 V vs. RHE. Note that STEM videos were acquired without potential applied from -40 to 0 s in order to show no beam-induced damage at a dose rate of ~12.5 e^-/nm^2s. A potential of -0.8 V vs. RHE was applied from 0 to 56 s.

Supplementary Video 5. *Operando* EC-STEM videos of 10 nm NP ensemble at -0.8 V vs. RHE for about 30 s. Note that STEM videos were acquired without potential applied from -16 to 0 s in order to show no beam-induced damage at a dose rate of ~5 e^-/nm^2s. A potential of -0.8 V vs. RHE was applied from 0 to 84 s.

Supplementary Video 6. *Operando* EC-STEM videos of 18 nm NP ensemble at -0.8 V vs. RHE for an extended time period of ~4 min at a dose rate of ~5 e^-/nm^2s.

Supplementary Video 7. *Operando* EC-STEM videos of 5 nm NP ensemble at -0.8 V vs. RHE for 60 s. Note that STEM videos were acquired without potential applied from -40 to 0 s in order to show no beam-induced damage at a dose rate of ~12.5 e^-/nm^2s. A potential of -0.8 V vs. RHE was applied from 0 to 60 s.